Activity patterns in ring networks of quadratic integrate-and-fire neurons with synaptic and gap junction coupling

Oleh E. Omel'chenko[1, *] and Carlo R. Laing[2, †]

[1] *University of Potsdam, Institute of Physics and Astronomy,*
Karl-Liebknecht-Str. 24/25, 14476 Potsdam, Germany
[2] *School of Mathematical and Computational Sciences,*
Massey University, Private Bag 102-904 NSMC, Auckland, New Zealand
(Dated: November 5, 2024)

We consider a ring network of quadratic integrate-and-fire neurons with nonlocal synaptic and gap junction coupling. The corresponding neural field model supports solutions such as standing and travelling waves, and also lurching waves. We show that many of these solutions satisfy self-consistency equations which can be used to follow them as parameters are varied. We perform numerical bifurcation analysis of the neural field model, concentrating on the effects of varying gap junction coupling strength. Our methods are generally applicable to a wide variety of networks of quadratic integrate-and-fire neurons.

I. INTRODUCTION

The collective behaviour of spatially extended networks of neurons is a topic of ongoing interest [1–6]. While it is possible to simulate large networks of model neurons [7, 8], continuum level descriptions (neural field models) often provide more potential for mathematical analysis. Early neural field models were phenomenological [9–12] but more recently models derived rigorously from infinite networks of spiking neurons have become available [13–19].

One type of solution of a neural field model is a "bump" — a spatially localised group of active neurons. Such solutions are thought to be relevant to working memory [20] and the head direction system [21, 22]. Also important are travelling waves [23–26]. These are thought to be relevant for modelling epilepsy and migraines, see for example [27]. We are often interested in when and how such solutions lose stability or are destroyed in bifurcations, and what patterns are stable beyond such bifurcations. For example, a bump may start to "breathe" [28] or a travelling wave may no longer have a fixed profile.

In this paper we study a ring network of quadratic integrate-and-fire (QIF) neurons coupled both synaptically and via gap junctions. We analyse the continuum network, whose dynamics are described by a neural field model. In similar previous work we considered networks of theta neurons with just synaptic coupling, concentrating on only time-periodic solutions [16]. (The QIF neuron with infinite threshold and reset is equivalent to a theta neuron [29].) In earlier work we also studied the stationary states of a ring network of synaptically coupled theta neurons [14]. On the other hand, models similar (but not identical) to ours have been the focus of other reasearchers. Byrne et al. studied networks of QIF neurons with both synaptic and gap junction coupling, but their synaptic coupling incorporated propagation delays and the gap junction coupling was purely local [5]. Their neural field model was only valid in the long wavelength limit. Schmidt and Avitabile considered a ring network of QIF neurons with nonlocal synaptic coupling and analysed both steady states and time dependent solutions which arose as the result of periodic forcing [18]. Esnaola-Acebes et al. studied a similar model, focussing on the decaying oscillatory modes that such models show [17]. Byrne et al. also considered a ring network of QIF neurons with synaptic coupling, performing a largely numerical study of some of the possible types of solutions [19].

Our model is probably most similar to that of [5], but one of our contributions is to show that some solutions of interest can be analysed using a self-consistency approach that has previously been used only for networks of theta neurons or Kuramoto and Winfree oscillators [16, 30, 31]. The structure of the paper is as follows. In Sec. II we present the model and describe the types of patterns typically seen when numerically solving it. In Sec. III we choose two values of the synaptic coupling strength and vary the strength of the gap junction coupling, observing transitions between various types of solutions. In Sec. IV we present analytical methods which can be used to describe most of the solutions observed in Sec. III. Section V shows the results of implementing the methods described in Sec. IV and includes a discussion of the relative efficiencies of several alternative methods. We conclude in Sec. VI, and the Appendix contains a number of useful results about the solutions of the complex Riccati equation.

---

* omelchenko@uni-potsdam.de
† c.r.laing@massey.ac.nz

II. MODEL AND TYPES OF SOLUTIONS

Let us consider a spatially extended network of N quadratic integrate-and-fire (QIF) neurons with both gap-junction and pulsatile synaptic coupling:

$$\frac{dV_j}{dt} = \eta_j + V_j^2 + \kappa_{\mathrm{v}}\ell \sum_{k=1}^{N} W_{\mathrm{v}}\left(|j-k|\ell\right)(V_k - V_j) + \kappa_{\mathrm{s}}\ell \sum_{k=1}^{N}\sum_{m\in\mathbb{Z}} W_{\mathrm{s}}\left(|j-k|\ell\right)\delta\left(t - T_k^m\right). \tag{1}$$

Here, the spiking events of the jth neuron T_j^m are determined by the reset condition: if $V_j \to +\infty$ for $t \nearrow T_j^m$, then $V_j \to -\infty$ for $t \searrow T_j^m$.

We assume that the network is organized as a one-dimensional array with periodic boundary conditions and distance-dependent connectivity defined by coupling functions W_{v} and W_{s}. The neurons differ from each other only in the excitability parameters η_j, which are chosen randomly and independently from a Lorentzian distribution

$$g(\eta) = \frac{1}{\pi}\frac{\gamma}{(\eta - \eta_0)^2 + \gamma^2} \quad \text{with} \quad \eta_0 \in \mathbb{R} \quad \text{and} \quad \gamma > 0.$$

The coupling functions W_{v} and W_{s} are assumed to be even, continuous and periodic

$$W_{\mathrm{v}}\left((k+N)\ell\right) = W_{\mathrm{v}}\left(k\ell\right), \qquad W_{\mathrm{s}}\left((k+N)\ell\right) = W_{\mathrm{s}}\left(k\ell\right),$$

and the intensity of interactions between neurons is controlled by two scalar coupling strengths κ_{v} and κ_{s}. Moreover, for the sake of simplicity of the analytical consideration below, it is convenient to assume $\ell = 2\pi/N$. In this case, functions $W_{\mathrm{v}}(x)$ and $W_{\mathrm{s}}(x)$ are 2π-periodic and can be represented in the form of Fourier series

$$W_{\mathrm{v}}(x) = \sum_{m=-\infty}^{\infty} \hat{W}_{\mathrm{v},m} e^{imx} \quad \text{and} \quad W_{\mathrm{s}}(x) = \sum_{m=-\infty}^{\infty} \hat{W}_{\mathrm{s},m} e^{imx}$$

with coefficients

$$\hat{W}_{\mathrm{v},m} = \frac{1}{2\pi}\int_{-\pi}^{\pi} W_{\mathrm{v}}(x) e^{-imx} dx \quad \text{and} \quad \hat{W}_{\mathrm{s},m} = \frac{1}{2\pi}\int_{-\pi}^{\pi} W_{\mathrm{s}}(x) e^{-imx} dx. \tag{2}$$

Note that for even functions $W_{\mathrm{v}}(x)$ and $W_{\mathrm{s}}(x)$, the coefficients $\hat{W}_{\mathrm{v},m}$ and $\hat{W}_{\mathrm{s},m}$ are real and therefore

$$\hat{W}_{\mathrm{v},m} = \frac{1}{2\pi}\int_{-\pi}^{\pi} W_{\mathrm{v}}(x)\cos(mx) dx \quad \text{and} \quad \hat{W}_{\mathrm{s},m} = \frac{1}{2\pi}\int_{-\pi}^{\pi} W_{\mathrm{s}}(x)\cos(mx) dx.$$

It is well-known [5, 13, 29, 32, 33] that in the continuum limit $N \to \infty$, the long-term dynamics of system (1) can be described by a neural field equation

$$\frac{\partial u}{\partial t} = \gamma - \kappa_{\mathrm{v}} u + i\left[\eta_0 + \kappa_{\mathrm{v}}\mathcal{K}_{\mathrm{v}}\mathrm{Im}\left(u\right) + \frac{\kappa_{\mathrm{s}}}{\pi}\mathcal{K}_{\mathrm{s}}\mathrm{Re}\left(u\right) - u^2\right] \tag{3}$$

for a complex-valued function $u = u(x,t)$, where $\mathcal{K}_{\mathrm{v}}$ and $\mathcal{K}_{\mathrm{s}}$ denote two integral operators

$$(\mathcal{K}_{\mathrm{v}}\varphi)(x) = \int_0^{2\pi} W_{\mathrm{v}}(x-y)\varphi(y) dy \quad \text{and} \quad (\mathcal{K}_{\mathrm{s}}\varphi)(x) = \int_0^{2\pi} W_{\mathrm{s}}(x-y)\varphi(y) dy.$$

Note that the real and imaginary parts of the solution $u(x,t)$ can be related to the local firing rate

$$R(x,t) = \frac{1}{\pi}\mathrm{Re}\, u(x,t) \tag{4}$$

and the local mean field potential

$$V(x,t) = \mathrm{Im}\, u(x,t). \tag{5}$$

Due to this interpretation, only those solutions that satisfy $\mathrm{Re}\,(u) \geq 0$ are physically meaningful. Moreover, it can be explicitly shown that the property $\mathrm{Re}\,(u) \geq 0$ is preserved by the dynamics of Eq. (3). Therefore, we focus on this invariant set below.

Note also that the mapping

$$z(x,t) = \frac{1 - \overline{u}}{1 + \overline{u}},\tag{6}$$

where overline denotes the complex conjugate, transforms the function u into an analog of the Kuramoto local order parameter, z; the dynamics can be written equally-well in terms of z [5, 13].

In the examples below, we choose $W_v(x)$ in the form of a Gaussian function

$$W_v(x) = \frac{1}{\sqrt{2\pi}\sigma}e^{-x^2/(2\sigma^2)} \quad \text{with} \quad \sigma = 0.1,\tag{7}$$

and $W_s(x)$ in the form of a Mexican-hat function which is positive for small $|x|$ and negative for larger $|x|$:

$$W_s(x) = \frac{1}{\sqrt{2\pi}\sigma_1}e^{-x^2/(2\sigma_1^2)} - \frac{1}{\sqrt{2\pi}\sigma_2}e^{-x^2/(2\sigma_2^2)} \quad \text{with} \quad \sigma_1 = 0.5,\ \sigma_2 = 1.\tag{8}$$

More precisely, the above functions determine the coupling only for $|x| \leq \pi$, while we use their 2π-periodic extensions for other values of x. Note that the width of the gap junction coupling kernel, W_v, is much smaller than that of the synaptic coupling kernel, W_s, since gap junctional coupling is typically more localised than synaptic coupling [13].

In numerical simulations for the spatially discretized version of Eq. (3), we usually encountered the following five types of stable states:

1. Uniform states, i.e. constant solutions of Eq. (3) that do not depend on either x or t.

2. Stationary states, i.e. time-independent solutions of the form $u = a(x)$ for some 2π-periodic function a.

3. Traveling waves, i.e. solutions of the form $u = a(x - st)$, which are stationary in a frame moving with a constant speed $s \neq 0$.

4. Standing waves, i.e. solutions $u = a(x,t)$ satisfying the periodicity condition $a(x, t + T) = a(x,t)$ with some $T > 0$.

5. Lurching waves, i.e. solutions $u = a(x,t)$ satisfying the shifted periodicity condition $a(x + \chi, t + T) = a(x,t)$ with some $\chi \neq 0$ and $T > 0$. Such waves have been found previously in neural models [34–39].

In this paper we analyse all of these types of solutions using a mixture of numerical and analytical methods. In Sec. III we show examples of these types of solution and characterise some aspects of them as the parameter κ_v (the strength of gap junction coupling) is varied. We choose to vary this parameter as the influence of gap junction coupling in neural field models has only recently been considered [13, 32, 33]. In Sec. IV we undertake bifurcation analysis of the various types of solution, sometimes describing them using a recently presented method that can be used to efficiently characterise solutions using self-consistency arguments [16, 30, 31, 40].

III. PHENOMENOLOGY

To determine the typical attractors of the neural field equation (3), we discretized it on a uniform spatial grid of 1024 nodes and performed numerical simulations for various parameters κ_s and κ_v. Other parameters were chosen as $\eta_0 = 1$ and $\gamma = 0.5$, by analogy with a similar model considered by Byrne et al. in [5]. Our observations are summarized below, where we provide a comprehensive overview of two representative cases $\kappa_s = 10$ and $\kappa_s = 20$.

A. Case $\kappa_s = 10$

Choosing $\eta_0 = 1$, $\gamma = 0.5$, $\kappa_s = 10$ and $\kappa_v = 1$ and running the numerical simulations for Eq. (3) with various initial conditions, we found two coexisting spatio-temporal patterns; see Fig. 1. One of them had the appearance of a periodically oscillating standing wave, while the other had the appearance of a travelling wave, although the wave does not travel with a constant profile. Note that standing and travelling waves have been observed in several other neural field models [5, 16, 19].

Next, by adiabatically changing the coupling strength κ_v, we investigated the stability intervals of these patterns. (When moving from one value of κ_v to the next, we added a small random perturbation to the final state to give the
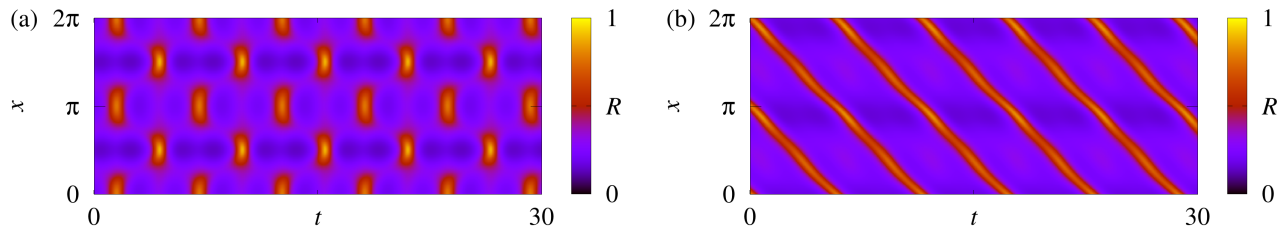
FIG. 1. (a) A standing wave solution of Eq. (3) and (b) a coexisting travelling wave solution. For both states, the local firing rate R, calculated by formula (4), is shown. Parameters: $\kappa_{\mathrm{s}} = 10$, $\kappa_{\mathrm{v}} = 1$, $\eta_0 = 1$ and $\gamma = 0.5$.

new initial state.) To this end, for each value of κ_{v}, we calculated a trajectory of length 1000 time units, discarding the previous transient of the same length. To characterize the dynamics of the obtained trajectory, we used the spatially averaged firing rate

$$\langle R(t) \rangle = \frac{1}{2\pi} \int_0^{2\pi} R(x,t)dx = \frac{1}{2\pi^2} \int_0^{2\pi} \mathrm{Re}\, u(x,t)dx$$

and its time variation

$$\Delta R = \max_t \langle R(t) \rangle - \min_t \langle R(t) \rangle.$$

where t runs over the length of the simulation. In the case $\Delta R > 0$, i.e. when $\langle R(t) \rangle$ is non-constant, we used the plot of $\langle R(t) \rangle$ to calculate the time intervals Δt between consecutive local maxima of this function. The resulting dependences of ΔR and Δt on κ_{v} are shown in Fig. 2. Moreover, for every time-periodic solution of Eq. (3), we also show its least period T, which was calculated by averaging the time intervals between the consecutive local maxima of $\mathrm{Re}\, u(0,t)$. (Note that for travelling waves we needed to double the above value, since $\mathrm{Re}\, u(0,t)$ attains two maxima during the period. Moreover, for travelling waves with $\kappa_{\mathrm{v}} > 0.964$ we also took into account that additional local maxima with $\mathrm{Re}\ u(0,t) < 1.5$ occur between the primary local maxima of $\mathrm{Re}\ u(0,t)$.)

The diagrams in the left column of Fig. 2 indicate the existence of two types of standing waves: the waves with a single maximal value of $\langle R(t) \rangle$ and the waves with two alternating maximal values of $\langle R(t) \rangle$. Typical examples of these patterns are shown in Fig. 3.

The diagrams in the right column of Fig. 2 have a more complicated structure. There, we can distinguish four different types of travelling waves, see Fig. 4. The left-most values of κ_{v} correspond to a wave that moves rigidly (notice $\Delta R = 0$) with a constant speed (Fig. 4(a)). For a larger value of κ_{v}, we found a wave propagating with a non-constant profile, which slowly drifts (Fig. 4(b)). This is a *lurching* wave. For a still larger value of κ_{v} the lurching wave undergoes some form of quasiperiodic modulation (Fig. 4(c)). Finally, for the right-most values of κ_{v}, we observe a wave moving above a turbulent background (Fig. 4(d)).

B. Case $\kappa_{\mathrm{s}} = 20$

Keeping $\eta_0 = 1$, $\gamma = 0.5$ and setting $\kappa_{\mathrm{s}} = 20$ we obtain several new types of solution for different values of κ_{v}; see Fig. 5. We see "two-bump" stationary solutions, Fig. 5(a), for which there are two disjoint regions where neurons are firing at a significant rate [10, 41]. We also see standing waves (or "breathing" two-bump solutions, similar to those seen in [13, 18, 19]), Fig. 5(b), more complex standing wave solutions, Fig. 5(c), lurching waves, Fig. 5(d), and waves that travel but are not periodic in a uniformly-travelling coordinate frame, Fig. 5(e,f). Quasi-statically sweeping through κ_{v} we obtain Fig. 6.

In the rest of the paper we analyse the types of solution shown, and provide a more rigorous explanation for the results observed above.

IV.   ANALYTICAL METHODS

The kaleidoscopic set of spatiotemporal patterns found in Eq. (3) for various system parameters can be logically explained by a bifurcation analysis of this equation, focusing on its equilibrium and periodic solutions. We describe two ways to do this. Our first approach relies on a discretized version of the integro-differential equation (3) and uses a
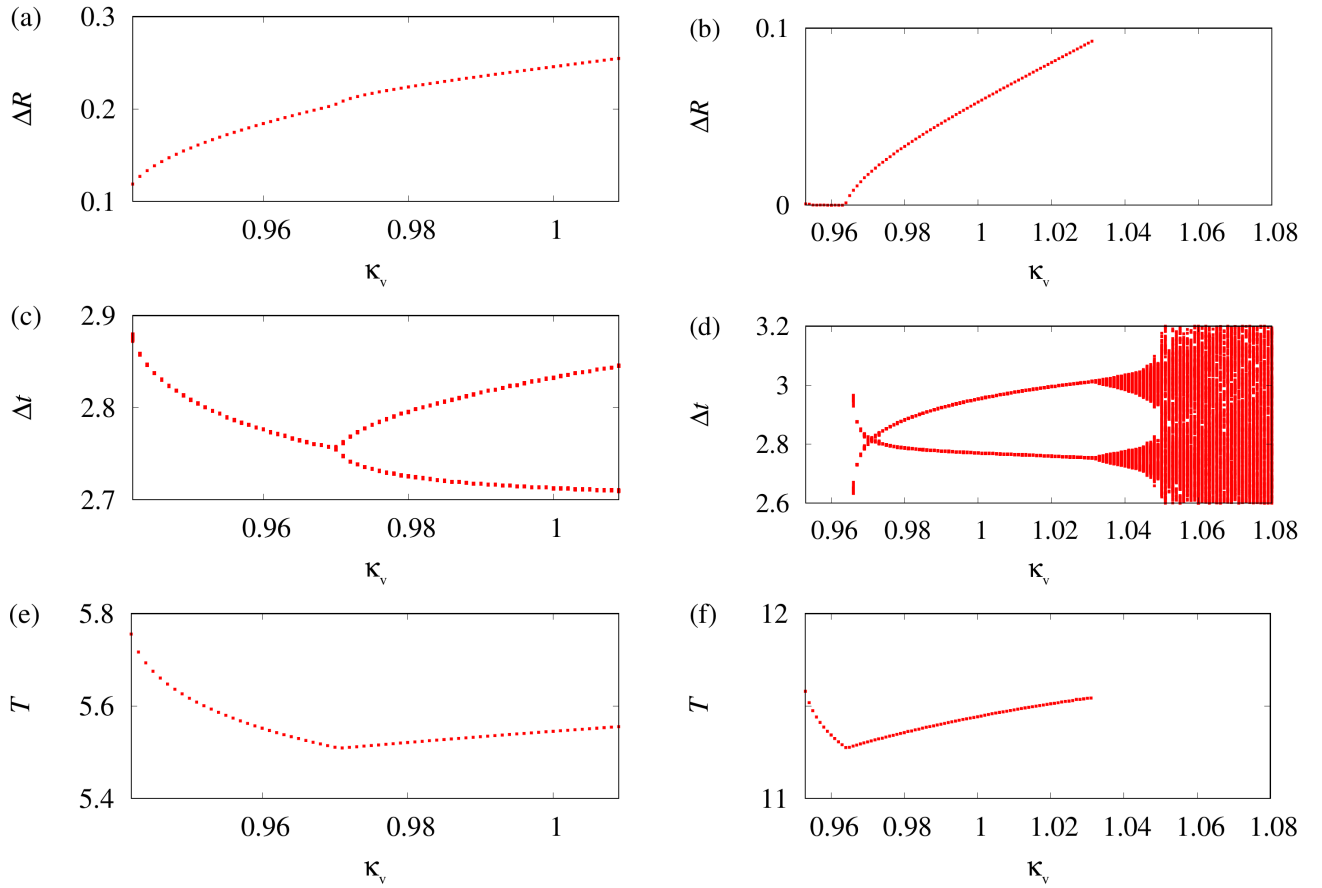
FIG. 2. Parameter sweeps of standing wave (left column) and travelling wave (right column) solutions of Eq. (3). Three rows show the time variation of spatially averaged firing rate ΔR, the time intervals Δt between the consecutive local maxima in the plot of $\langle R(t) \rangle$, and the least period T. Other parameters: $\eta_0 = 1$, $\gamma = 0.5$ and $\kappa_s = 10$.
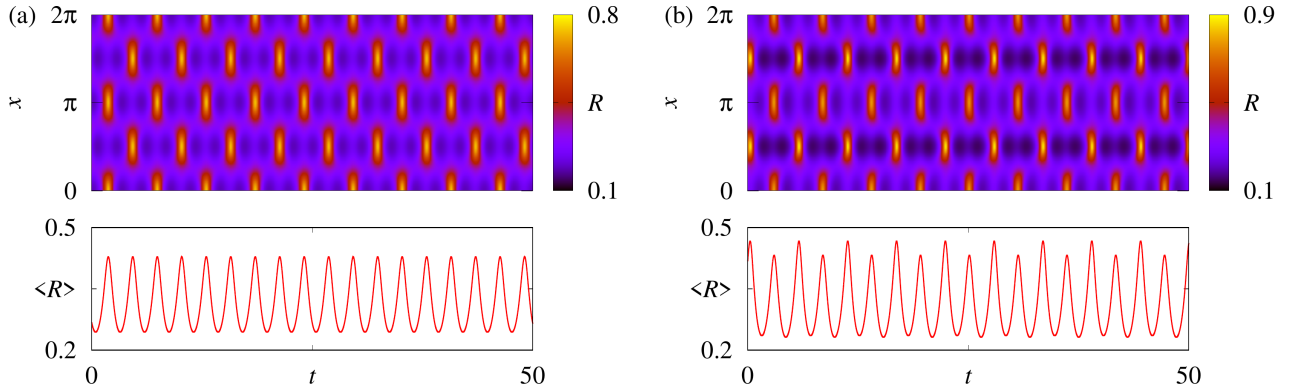

FIG. 3. Two types of standing wave solutions of Eq. (3) for $\kappa_v = 0.96$ (a) and $\kappa_v = 0.99$ (b). Other parameters: $\eta_0 = 1$, $\gamma = 0.5$ and $\kappa_s = 10$.

standard implementation in Matlab of pseudo-arclength continuation for the bifurcation analysis of finite-dimensional dynamical systems [42]. In the second approach, we derive a set of integral self-consistency equations for different types of solutions of Eq. (3) and carry out their finite-dimensional reduction by Galerkin method.
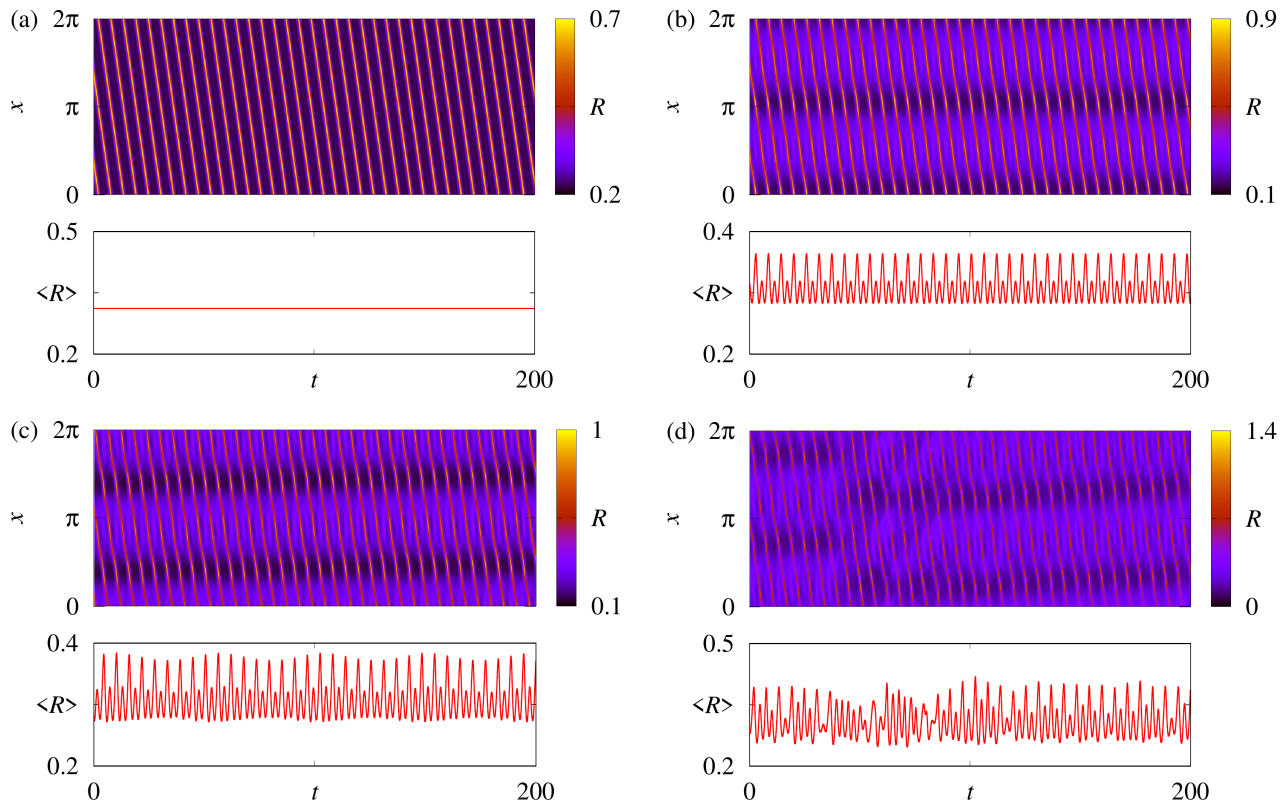
FIG. 4. Four types of travelling waves in Eq. (3) for $\kappa_{\mathrm{v}} = 0.96$ (a), $\kappa_{\mathrm{v}} = 1.02$ (b), $\kappa_{\mathrm{v}} = 1.04$ (c) and $\kappa_{\mathrm{v}} = 1.07$ (d). Other parameters: $\eta_0 = 1$, $\gamma = 0.5$ and $\kappa_{\mathrm{s}} = 10$.

A. Uniform states

We start with the simplest form of solution, a uniform state. Recall that these are constant solutions of Eq. (3), which do not depend on either x or t. On the other hand, these states will not be steady states of system (1), as that describes a finite network of heterogeneous spiking neurons. However, in system (1), such a state would have no macroscopic spatial structure nor significant temporal variations.

1. Existence

Each uniform state of Eq. (3) corresponds to a solution $u \in \mathbb{C}$ of the equation

$$\gamma - \kappa_{\mathrm{v}} u + i \left[\eta_0 + \kappa_{\mathrm{v}} \mathcal{K}_{\mathrm{v}} \mathrm{Im}\,(u) + \frac{\kappa_{\mathrm{s}}}{\pi} \mathcal{K}_{\mathrm{s}} \mathrm{Re}\,(u) - u^2 \right] = 0. \tag{9}$$

In the next proposition, we show that all physically meaningful solutions of Eq. (9) lie on a certain one-parameter manifold.

Proposition 1 *All constant solutions of Eq. (9) satisfying* $\mathrm{Re}\,(u) \geq 0$ *lie on the manifold defined by formulas*

$$u = \frac{1}{2} f_-(F, \kappa_{\mathrm{v}}, \gamma) + \frac{i}{2} \left(\kappa_{\mathrm{v}} - f_+(F, \kappa_{\mathrm{v}}, \gamma) \right), \tag{10}$$

$$\eta_0 = F - \pi \kappa_{\mathrm{v}} \hat{W}_{\mathrm{v},0} \left(\kappa_{\mathrm{v}} - f_+(F, \kappa_{\mathrm{v}}, \gamma) \right) - \kappa_{\mathrm{s}} \hat{W}_{\mathrm{s},0} f_-(F, \kappa_{\mathrm{v}}, \gamma), \tag{11}$$

where

$$f_{\pm}(F, \kappa_{\mathrm{v}}, \gamma) = \sqrt{\frac{\sqrt{(\kappa_{\mathrm{v}}^2 - 4F)^2 + 16\gamma^2} \pm (\kappa_{\mathrm{v}}^2 - 4F)}{2}},$$

the coefficients $\hat{W}_{\mathrm{v},0}$ and $\hat{W}_{\mathrm{s},0}$ are defined by the formula (2) with $m = 0$, and $F \in \mathbb{R}$ is a free parameter.
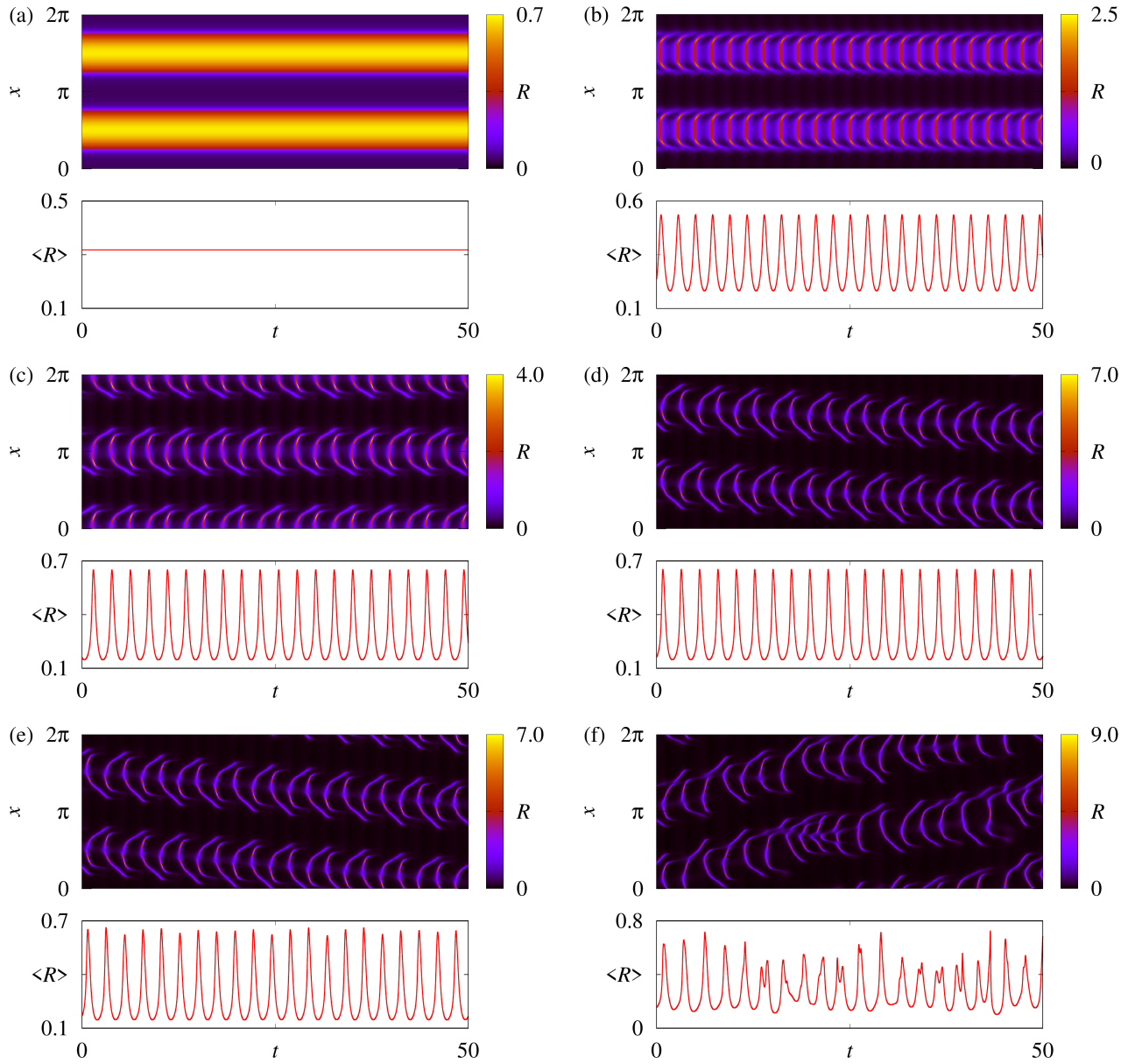
FIG. 5. Six types of solutions of Eq. (3) for $\kappa_\mathrm{v} = 0.8$ (a), $\kappa_\mathrm{v} = 1$ (b), $\kappa_\mathrm{v} = 1.3$ (c), $\kappa_\mathrm{v} = 1.6$ (d), $\kappa_\mathrm{v} = 1.65$ (e) and $\kappa_\mathrm{v} = 1.8$ (f). Other parameters: $\eta_0 = 1$, $\gamma = 0.5$ and $\kappa_\mathrm{s} = 20$.

Proof: Let us rewrite Eq. (9) in the form

$$\gamma + iF - \kappa_\mathrm{v} u - iu^2 = 0, \tag{12}$$

where

$$F = \eta_0 + \kappa_\mathrm{v} \mathcal{K}_\mathrm{v} \mathrm{Im}\,(u) + \frac{\kappa_\mathrm{s}}{\pi} \mathcal{K}_\mathrm{s} \mathrm{Re}\,(u). \tag{13}$$

For a given F, Eq. (12) has one and only one solution satisfying $\mathrm{Re}\,(u) \geq 0$, see Proposition 3. It is determined by
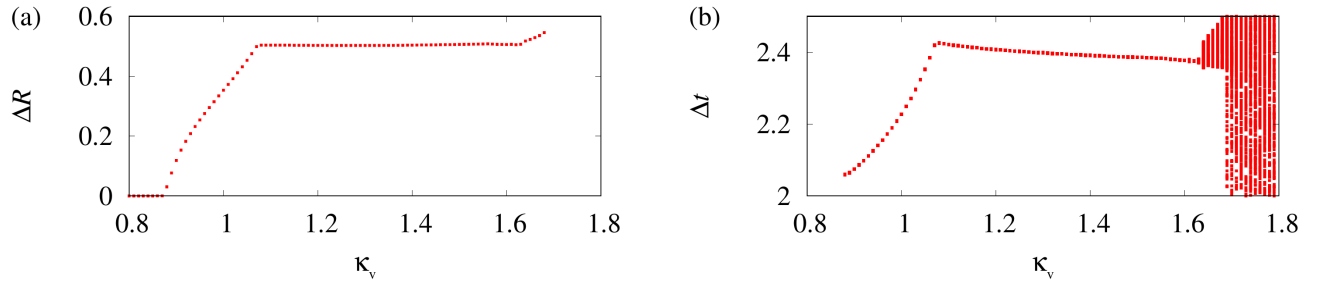
FIG. 6. A parameter sweep for patterned solutions shown in Fig. 5. The panels (a) and (b) show the time variation of spatially averaged firing rate ΔR and the time intervals Δt between the consecutive local maxima in the plot of $\langle R(t) \rangle$, respectively. Other parameters: $\eta_0 = 1$, $\gamma = 0.5$ and $\kappa_\mathrm{s} = 20$.

the formula (10). Inserting this result into Eq. (13) we obtain

$$
F = \eta_0 + \pi \kappa_\mathrm{v} \hat{W}_{\mathrm{v},0} \left(\kappa_\mathrm{v} - \sqrt{\frac{\sqrt{(\kappa_\mathrm{v}^2 - 4F)^2 + 16\gamma^2} + \kappa_\mathrm{v}^2 - 4F}{2}} \right)
$$

$$
+ \kappa_\mathrm{s} \hat{W}_{\mathrm{s},0} \sqrt{\frac{\sqrt{(\kappa_\mathrm{v}^2 - 4F)^2 + 16\gamma^2} - \kappa_\mathrm{v}^2 + 4F}{2}},
$$

what is an equivalent form of (11). ∎

Note that Proposition 1 allows us to explicitly express the dependence of the constant solution u on the parameter η_0 (albeit, in a parametric form). The same applies to the dependence of u on κ_s, if $\hat{W}_{\mathrm{s},0} \neq 0$.

2. Linear stability

Suppose that $u_0 \in \mathbb{C}$ is a constant solution of Eq. (9). To analyze its stability, we insert the ansatz $u(x,t) = u_0 + v(x,t)$ into Eq. (9) and linearize the resulting equation with respect to small perturbations $v(x,t)$. This yields a linear integro-differential equation

$$
\frac{\partial v}{\partial t} = \mu v + \frac{\kappa_\mathrm{v}}{2} \mathcal{K}_\mathrm{v}(v - \overline{v}) + \frac{i\kappa_\mathrm{s}}{2\pi} \mathcal{K}_\mathrm{s}(v + \overline{v}), \tag{14}
$$

where

$$
\mu = -\kappa_\mathrm{v} - 2iu_0. \tag{15}
$$

Remark 1 *If* $\mathrm{Re}\,(u_0) \geq 0$ *and hence* u_0 *is determined by Proposition 1, then* $\mathrm{Re}\,(\mu) < 0$. *Indeed, this inequality is easy to verify by inserting the* u_0 *defined by formula (10) into (15).*

To investigate the growth or decay of different spatial modes, we insert the ansatz

$$
v(x,t) = v_+(x)e^{\lambda t} + \overline{v}_-(x)e^{\overline{\lambda} t}
$$

into Eq. (14) and equate separately the terms at $e^{\lambda t}$ and $e^{\overline{\lambda} t}$. Thus, we obtain a spectral problem

$$
\lambda v_+ = \mu v_+ + \frac{\kappa_\mathrm{v}}{2} \mathcal{K}_\mathrm{v}(v_+ - v_-) + \frac{i\kappa_\mathrm{s}}{2\pi} \mathcal{K}_\mathrm{s}(v_+ + v_-), \tag{16}
$$

$$
\lambda v_- = \overline{\mu} v_- - \frac{\kappa_\mathrm{v}}{2} \mathcal{K}_\mathrm{v}(v_+ - v_-) - \frac{i\kappa_\mathrm{s}}{2\pi} \mathcal{K}_\mathrm{s}(v_+ + v_-). \tag{17}
$$

Now, we analyze the properties of spatial Fourier modes

$$
(v_+(x), v_-(x))^\mathrm{T} = (V_+, V_-)^\mathrm{T} e^{imx} \quad \text{with} \quad m \in \mathbb{Z} \quad \text{and} \quad (V_+, V_-)^\mathrm{T} \in \mathbb{C}^2.
$$

Inserting this ansatz into Eqs. (16), (17) and using the identities

$$\mathcal{K}_{\mathrm{v}}e^{imx} = 2\pi\hat{W}_{\mathrm{v},m}e^{imx} \quad \text{and} \quad \mathcal{K}_{\mathrm{s}}e^{imx} = 2\pi\hat{W}_{\mathrm{s},m}e^{imx}$$

with the coefficients $\hat{W}_{\mathrm{v},m}$ and $\hat{W}_{\mathrm{s},m}$ defined by (2), we obtain a linear system

$$\lambda V_+ = \mu V_+ + \pi\kappa_{\mathrm{v}}\hat{W}_{\mathrm{v},m}(V_+ - V_-) + i\kappa_{\mathrm{s}}\hat{W}_{\mathrm{s},m}(V_+ + V_-),$$

$$\lambda V_- = \overline{\mu}V_- - \pi\kappa_{\mathrm{v}}\hat{W}_{\mathrm{v},m}(V_+ - V_-) - i\kappa_{\mathrm{s}}\hat{W}_{\mathrm{s},m}(V_+ + V_-).$$

Its characteristic equation reads

$$\lambda^2 - 2\lambda\mathrm{Re}\,(\mu + P_m) + |\mu + P_m|^2 - |P_m|^2 = 0$$

where

$$P_m = \pi\kappa_{\mathrm{v}}\hat{W}_{\mathrm{v},m} + i\kappa_{\mathrm{s}}\hat{W}_{\mathrm{s},m}.$$

Solving this equation, we obtain

$$\lambda_\pm = \mathrm{Re}\,(\mu + P_m) \pm \sqrt{|P_m|^2 - (\mathrm{Im}\,(\mu + P_m))^2}$$

$$= \mathrm{Re}\,(\mu) + \pi\kappa_{\mathrm{v}}\hat{W}_{\mathrm{v},m} \pm \sqrt{\pi^2\kappa_{\mathrm{v}}^2\hat{W}_{\mathrm{v},m}^2 + \kappa_{\mathrm{s}}^2\hat{W}_{\mathrm{s},m}^2 - \left(\mathrm{Im}\,(\mu) + \kappa_{\mathrm{s}}\hat{W}_{\mathrm{s},m}\right)^2}.$$

Since the Fourier coefficients of $W_{\mathrm{v}}(x)$ and $W_{\mathrm{s}}(x)$ always satisfy the decay property $|\hat{W}_{\mathrm{v},m}|, |\hat{W}_{\mathrm{s},m}| \to 0$ for $|m| \to \infty$, this means $\lambda_\pm \to \mu$ or $\lambda_\pm \to \overline{\mu}$ for $|m| \to \infty$. In other words, any potential instability of u_0 can be associated with relatively small indices m in the above formula for $\lambda_\pm$.

Instabilities of the uniform state for coupling functions (7), (8) and $m = 0, 1, 2, 3$ are shown in Fig. 7. Their position in the $(\kappa_{\mathrm{v}}, \kappa_{\mathrm{s}})$-plane indicates that only the modes with $m = 0$ and $m = 2$ determine stability boundaries. Note that along the curve $m = 0$, the critical eigenvalues everywhere have non-zero imaginary parts (at least for the range $\kappa_{\mathrm{s}} \in [0, 30]$). In contrast, on the curve $m = 2$ we find this property only for $\kappa_{\mathrm{s}} < 13.0$. Above this value, the pair of complex conjugate eigenvalues turns into a pair of real eigenvalues, so that the corresponding stability boundary has a corner point. As a result, two qualitatively different bifurcation scenarios of the uniform state are expected for $\kappa_{\mathrm{s}} < 13.0$ and $\kappa_{\mathrm{s}} > 13.0$. Indeed, for $\kappa_{\mathrm{s}} = 10$ the uniform state with $\mathrm{Re}\,(u) \geq 0$ is stable to the left of the $m = 0$ curve and as κ_{v} increases, a Hopf bifurcation occurs, which leads to the creation of a time-dependent (but still spatially uniform) solution. However, for $\kappa_{\mathrm{s}} = 20$ the uniform state loses stability to the $m = 2$ mode as κ_{v} is increased. The eigenvalues corresponding to this instability are real, so this is a Turing bifurcation creating a stationary spatial pattern.

FIG. 7. (a) Stability boundaries of the uniform state of Eq. (3) determined by the condition $\max(\mathrm{Re}\lambda_+, \mathrm{Re}\lambda_-) = 0$ for $m = 0, 1, 2$ and 3. The uniform state is stable in the lower left region, bounded by the $m = 0$ and $m = 2$ curves. (b) Enlargement of the range around $\kappa_{\mathrm{v}} = 1$. Note that as κ_s increases above 13.0, the pair of complex conjugate eigenvalues for $m = 2$ turns into a pair of real eigenvalues, so that the corresponding stability boundary has a corner point. Other parameters: $\eta_0 = 1$ and $\gamma = 0.5$.

B. Stationary states

Stationary spatial patterns are non-constant time-independent solutions of Eq. (3), see Fig. 5(a). We can find them by solving a discretized version of Eq. (3). Alternatively, we can find them using a self-consistency equation we are about to derive. For this, we insert the ansatz $u = a(x)$ into Eq. (3) and obtain

$$\gamma + iF(x) - \kappa_{\mathrm{v}}a(x) - ia^2(x) = 0, \tag{18}$$

where

$$F(x) = \eta_0 + \kappa_{\mathrm{v}}\mathcal{K}_{\mathrm{v}}\mathrm{Im}\,(a) + \frac{\kappa_{\mathrm{s}}}{\pi}\mathcal{K}_{\mathrm{s}}\mathrm{Re}\,(a). \tag{19}$$

Using Proposition 3, we can solve Eq. (18) for each x separately

$$a(x) = \mathcal{S}(F(x), \kappa_{\mathrm{v}}, \gamma). \tag{20}$$

Then, inserting the result into Eq. (19), we obtain a self-consistency equation

$$F(x) = \eta_0 + \kappa_{\mathrm{v}}\mathcal{K}_{\mathrm{v}}\mathrm{Im}\left(\mathcal{S}\left(F(x), \kappa_{\mathrm{v}}, \gamma\right)\right) + \frac{\kappa_{\mathrm{s}}}{\pi}\mathcal{K}_{\mathrm{s}}\mathrm{Re}\left(\mathcal{S}\left(F(x), \kappa_{\mathrm{v}}, \gamma\right)\right). \tag{21}$$

Note that Eq. (21) should be solved with respect to the unknown function $F(x)$, which, in turn, determines the corresponding stationary state $a(x)$ by formula (20). By construction this procedure allows us to find all stationary states satisfying $|a(x)| \le 1$, while every unphysical state that violates this inequality for at least some x is automatically discarded.

In general, Eq. (21) cannot be solved exactly but only approximately. Given that $F(x)$ is real and 2π-periodic, it is convenient to approximate it using a truncated Fourier series

$$F(x) = \sum_{m=0}^{2M} \hat{f}_m \phi_m(x) \quad \text{with} \quad \hat{f}_m \in \mathbb{R}, \tag{22}$$

where

$$\begin{aligned} \phi_0(x) &= 1, \\ \phi_m(x) &= \sqrt{2}\cos((m+1)x/2) \text{ for odd } m, \\ \phi_m(x) &= \sqrt{2}\sin(mx/2) \text{ for even } m, \end{aligned} \tag{23}$$

are elements of the L^2-orthogonal trigonometric basis. Inserting this ansatz into Eq. (21) and projecting the resulting relation onto the basis function $\phi_m(x)$, we obtain a system of equations

$$\hat{f}_m = \eta_0\delta_{m0} + \int_0^{2\pi} \left[\kappa_{\mathrm{v}}\hat{W}_{\mathrm{v},m'}\mathrm{Im}\left(\mathcal{S}\left(F(x), \kappa_{\mathrm{v}}, \gamma\right)\right) + \frac{\kappa_{\mathrm{s}}}{\pi}\hat{W}_{\mathrm{s},m'}\mathrm{Re}\left(\mathcal{S}\left(F(x), \kappa_{\mathrm{v}}, \gamma\right)\right)\right]\phi_m(x)dx \tag{24}$$

for $m = 0, 1, 2, \ldots 2M$, where δ_{mn} is the Kronecker delta, $\hat{W}_{\mathrm{v},m}$ and $\hat{W}_{\mathrm{s},m}$ are the Fourier coefficients of $W_{\mathrm{v}}(x)$ and $W_{\mathrm{s}}(x)$ given by (2), and

$$m' = 0 \text{ if } m = 0, \quad m' = (m+1)/2 \text{ if } m \text{ is odd}, \quad m' = m/2 \text{ if } m \text{ is even}.$$

For completeness, we list here four identities

$$\int_0^{2\pi} (\mathcal{K}_{\mathrm{v}}u)(x)\cos(mx)dx = 2\pi\hat{W}_{\mathrm{v},m}\int_0^{2\pi} u(x)\cos(mx)dx, \tag{25}$$

$$\int_0^{2\pi} (\mathcal{K}_{\mathrm{v}}u)(x)\sin(mx)dx = 2\pi\hat{W}_{\mathrm{v},m}\int_0^{2\pi} u(x)\sin(mx)dx, \tag{26}$$

$$\int_0^{2\pi} (\mathcal{K}_{\mathrm{s}}u)(x)\cos(mx)dx = 2\pi\hat{W}_{\mathrm{s},m}\int_0^{2\pi} u(x)\cos(mx)dx, \tag{27}$$

$$\int_0^{2\pi} (\mathcal{K}_{\mathrm{s}}u)(x)\sin(mx)dx = 2\pi\hat{W}_{\mathrm{s},m}\int_0^{2\pi} u(x)\sin(mx)dx, \tag{28}$$

which are valid for arbitrary real function $u(x)$, any integer m, and any integral operators $\mathcal{K}_\mathrm{v}$ and $\mathcal{K}_\mathrm{s}$ with symmetric (even) kernels $W_\mathrm{v}(x)$ and $W_\mathrm{s}(x)$, respectively. We used these identities to obtain formula (24).

Note that for symmetric kernels $W_\mathrm{v}(x)$ and $W_\mathrm{s}(x)$ the dimensionality of system (24) can be halved. Indeed, it is easy to see that in this case the operators $\mathcal{K}_\mathrm{v}$ and $\mathcal{K}_\mathrm{s}$ are invariant on the subspace of even functions. Therefore, we can assume that $F(x)$ is even and hence $\hat{f}_m = 0$ for all even positive m. Importantly, after such an assumption we do not need to care about the translational symmetry of Eq. (21), which would otherwise require the addition of a pinning condition to (24).

In conclusion, we make a remark that for each stationary pattern $a(x)$ found using the self-consistency equation (21), its linear stability can be analyzed according to the scheme of Section IV A 2. For brevity, we do not perform such an analysis here, but note that conceptually this will not be very different from the linear stability analysis of bump states described in [14].

C. Travelling wave

In this section, we consider the traveling wave solutions of Eq. (3), which are uniformly drifting spatial patterns, see Fig. 4(a), with a mathematical form

$$u = a(x + st) \quad \text{where} \quad s \neq 0.$$

Our primary approach to studying them is to realise that such waves are stationary in a uniformly travelling coordinate system, travelling at the speed of the wave. Thus they are steady states of

$$\frac{\partial a}{\partial t} = \gamma - \kappa_\mathrm{v} a + i\left[\eta_0 + \kappa_\mathrm{v}\mathcal{K}_\mathrm{v}\mathrm{Im}\,(a) + \frac{\kappa_\mathrm{s}}{\pi}\mathcal{K}_\mathrm{s}\mathrm{Re}\,(a) - a^2\right] - s\frac{\partial a}{\partial x} \tag{29}$$

where s is the speed at which they travel [42, 43]. Thus we can find them by uniformly discretising (29) in space and solving the corresponding large set of coupled algebraic equations using Newton's method. The spatial derivative can be approximated using finite differences. One advantage of this method is that the stability of the wave can be determined from the eigenvalues of the linearisation of (29) about a steady state.

An alternative approach to the study of travelling waves in Eq. (3) consists in deriving a self-consistency equation for them. For this, we note that if $s > 0$ (which will be the default case below) and $a(x)$ is a time-independent solution of Eq. (29), then $a(x)$ satisfies

$$\frac{da}{dx} = \frac{\gamma}{s} + \frac{iF(x)}{s} - \frac{\kappa_\mathrm{v}}{s}a - \frac{i}{s}a^2, \tag{30}$$

where

$$F(x) = \eta_0 + \kappa_\mathrm{v}\mathcal{K}_\mathrm{v}\mathrm{Im}\,(a) + \frac{\kappa_\mathrm{s}}{\pi}\mathcal{K}_\mathrm{s}\mathrm{Re}\,(a).$$

For Eq. (30) we know (see Proposition 2 in Appendix) that for any $\gamma > 0$, $s > 0$, any $\kappa_\mathrm{v} \in \mathbb{R}$ and any real 2π-periodic function $F(x)$, this equation has one and only one 2π-periodic solution, which lies entirely in the right half-plane $\mathbb{P} = \{w \in \mathbb{C} : \mathrm{Re}\ w > 0\}$. Therefore, we can write

$$a(x) = \mathcal{U}(F(x), \kappa_\mathrm{v}, \gamma, s), \tag{31}$$

where $\mathcal{U}(\cdot)$ denotes the corresponding solution operator. To be consistent with the above definition of $F(x)$, we must have

$$F(x) = \eta_0 + \kappa_\mathrm{v}\mathcal{K}_\mathrm{v}\mathrm{Im}\,\left(\mathcal{U}\left(F(x), \kappa_\mathrm{v}, \gamma, s\right)\right) + \frac{\kappa_\mathrm{s}}{\pi}\mathcal{K}_\mathrm{s}\mathrm{Re}\,\left(\mathcal{U}\left(F(x), \kappa_\mathrm{v}, \gamma, s\right)\right). \tag{32}$$

Thus, in order to find a traveling wave solution of Eq. (3), we can first solve Eq. (32) for $F(x)$ and then use (31) to calculate the corresponding wave profile. Note that due to the translational symmetry of Eq. (3) we need to add an additional pinning condition such as

$$\int_0^{2\pi} F(x)\sin x\,dx = 0 \tag{33}$$

to pick up a unique solution of this equation. This condition also allows us to find the speed of traveling wave s.

Let us make a few remarks about the numerical implementation of the method based on the self-consistency equation (32). Recall that the algorithm for calculating the solution operator $\mathcal{U}(\cdot)$ is described in Remark 2 in Appendix. Moreover, the oprtimal strategy for solving Eq. (32) is the application of the Galerkin method. For this, we insert the ansatz (22) into Eq. (32) and project the resulting relation onto the trigonometric basis $\phi_m(x)$ defined in (23). As a result we obtain a system of $2M + 1$ equations

$$\hat{f}_m = \eta_0 \delta_{m0} + \int_0^{2\pi} \left[\kappa_{\mathrm{v}} \hat{W}_{\mathrm{v},m'} \mathrm{Im}\left(\mathcal{U}\left(F(x), \kappa_{\mathrm{v}}, \gamma, s\right)\right) + \frac{\kappa_{\mathrm{s}}}{\pi} \hat{W}_{\mathrm{s},m'} \mathrm{Re}\left(\mathcal{U}\left(F(x), \kappa_{\mathrm{v}}, \gamma, s\right)\right) \right] \phi_m(x) dx \qquad (34)$$

where

$$m' = 0 \text{ if } m = 0, \quad m' = (m+1)/2 \text{ if } m \text{ is odd}, \quad m' = m/2 \text{ if } m \text{ is even}.$$

Note that the solutions of Eq. (32) do not necessarily have to be reflection-symmetric, so all integer indices $m = 0, 1, \ldots, 2M$ must be taken into account in system (34). Moreover, in this case the pinning condition (33) cannot be omitted, although it becomes particularly simple

$$\hat{f}_2 = 0. \qquad (35)$$

Combining (34) with (35), we obtain a system that determines all $\hat{f}_m$ in (22) and the wave speed s.

D.   Standing wave

We use the term standing wave to refer to a spatiotemporal pattern that is non-constant in the spatial direction and exhibits periodic oscillation with the same collective period for each position x. Examples of such patterns are shown in Fig. 1(a), Fig. 3 and Fig. 5(b),(c). Mathematically, each standing wave corresponds to spatially heterogeneous periodic solution of Eq. (3), i.e. to a solution of the form $u = a(x,t)$ which is T-periodic in t for some $T > 0$. To study how these periodic solutions depend on system parameters, we can again use two approaches. On the one hand, we can look for periodic solutions of the discretized version of Eq. (3). On the other hand, we can derive a self-consistency equation similar to Eq. (21) and Eq. (32). To write such a self-consistency equation, we first perform time-rescaling, by defining a new unknown function $v(x,t) = u(x,t/\omega)$ where $\omega = 2\pi/T$ is the cyclic frequency corresponding to period T. The new function $v(x,t)$ satisfies

$$\omega \frac{\partial v}{\partial t} = \gamma - \kappa_{\mathrm{v}} v + i \left[\eta_0 + \kappa_{\mathrm{v}} \mathcal{K}_{\mathrm{v}} \mathrm{Im}\left(v\right) + \frac{\kappa_{\mathrm{s}}}{\pi} \mathcal{K}_{\mathrm{s}} \mathrm{Re}\left(v\right) - v^2 \right],$$

or equivalently

$$\frac{\partial v}{\partial t} = \frac{\gamma}{\omega} + \frac{iF(x,t)}{\omega} - \frac{\kappa_{\mathrm{v}}}{\omega} v - \frac{i}{\omega} v^2, \qquad (36)$$

where

$$F(x,t) = \eta_0 + \kappa_{\mathrm{v}} \mathcal{K}_{\mathrm{v}} \mathrm{Im}\left(v\right) + \frac{\kappa_{\mathrm{s}}}{\pi} \mathcal{K}_{\mathrm{s}} \mathrm{Re}\left(v\right). \qquad (37)$$

For every fixed $x \in [0, 2\pi]$, Eq. (36) has the same form as Eq. (30), but with other variables $x \mapsto t$ and $s \mapsto \omega$. Therefore, using the notation of the solution operator $\mathcal{U}(\cdot)$, we can write

$$v(x,t) = \mathcal{U}\left(F(x,t), \kappa_{\mathrm{v}}, \gamma, \omega\right). \qquad (38)$$

Inserting this into the definition of $F(x,t)$, we obtain a self-consistency equation

$$F(x,t) = \eta_0 + \kappa_{\mathrm{v}} \mathcal{K}_{\mathrm{v}} \mathrm{Im}\left(\mathcal{U}\left(F(x,t), \kappa_{\mathrm{v}}, \gamma, \omega\right)\right) + \frac{\kappa_{\mathrm{s}}}{\pi} \mathcal{K}_{\mathrm{s}} \mathrm{Re}\left(\mathcal{U}\left(F(x,t), \kappa_{\mathrm{v}}, \gamma, \omega\right)\right). \qquad (39)$$

Recalling that every solution $v_0(x,t)$ of the periodic boundary value problem for Eq. (36) determines a two-parameter familily of solutions $v_0(x + x_0, t + t_0)$ with $x_0, t_0 \in (0, 2\pi)$, we equip Eq. (39) with two additional pinning conditions

$$\int_0^{2\pi} \int_0^{2\pi} F(x,t) \sin x \, dx \, dt = \int_0^{2\pi} \int_0^{2\pi} F(x,t) \sin t \, dx \, dt = 0, \qquad (40)$$

which allow us to pick up a single function from this family.

In the following we use a Fourier sum approximation for $F(x,t)$:

$$F(x,t) = \sum_{m=0}^{2M} \sum_{n=0}^{2N} \hat{f}_{mn} \phi_m(x) \phi_n(t), \tag{41}$$

where $\hat{f}_{mn} \in \mathbb{R}$, and the ϕ_m are given in (23). Applying the standard Galerkin scheme to Eq. (39) we find a system of algebraic equations that determines the coefficients $\hat{f}_{mn}$:

$$\hat{f}_{mn} = \eta_0 \delta_{m0} \delta_{n0} + \left\langle \kappa_{\rm v} \mathcal{K}_{\rm v} {\rm Im} \left(\mathcal{U} \left(F(x,t), \kappa_{\rm v}, \gamma, \omega \right) \right) \right.$$
$$\left. + \frac{\kappa_{\rm s}}{\pi} \mathcal{K}_{\rm s} {\rm Re} \left(\mathcal{U} \left(F(x,t), \kappa_{\rm v}, \gamma, \omega \right) \right), \phi_m(x) \phi_n(t) \right\rangle \tag{42}$$

where

$$\langle u, v \rangle = \frac{1}{4\pi^2} \int_0^{2\pi} \int_0^{2\pi} u(x,t) \overline{v}(x,t) dx \, dt.$$

Moreover, using the identities (25)–(28), we simplify Eq. (42) to obtain

$$\hat{f}_{mn} = \eta_0 \delta_{m0} \delta_{n0} + \left\langle 2\pi \kappa_{\rm v} \hat{W}_{{\rm v},m'} {\rm Im} \left(\mathcal{U} \left(F(x,t), \kappa_{\rm v}, \gamma, \omega \right) \right) \right.$$
$$\left. + 2\kappa_{\rm s} \hat{W}_{{\rm s},m'} {\rm Re} \left(\mathcal{U} \left(F(x,t), \kappa_{\rm v}, \gamma, \omega \right) \right), \phi_m(x) \phi_n(t) \right\rangle, \tag{43}$$

where

$$m' = 0 \text{ if } m = 0, \quad m' = (m+1)/2 \text{ if } m \text{ is odd}, \quad m' = m/2 \text{ if } m \text{ is even.}$$

For the patterns shown in Fig. 1(a) and Fig. 3, we can, without loss of generality, assume $u(-x,t) = u(x,t)$ and hence $F(-x,t) = F(x,t)$. In this case, $\hat{f}_{mn} = 0$ for all even positive m. Therefore, the first pinning condition in (40) is satisfied automatically. For the second pinning condition, inserting the ansatz (41) into it, we obtain

$$\hat{f}_{02} = 0. \tag{44}$$

In summary, solving the system (43), (44) we are able to find an approximate solution $F(x,t)$ of the form (41) as well as the corresponding frequency ω. Then, by formula (38) we can calculate the solution of Eq. (36), which after the appropriate time rescaling $u(x,t) = v(x, \omega t)$ yields the standing wave solution of Eq. (3).

E. Lurching solutions

In this section, we consider lurching waves — the most complex type of solutions of Eq. (3) that we have been able to investigate analytically. A lurching wave is a travelling wave, but rather than having a constant profile, its profile periodically oscillates; see Fig. 1(b), Fig. 4(b) and Fig. 5(d). These are sometimes referred to as modulated travelling waves [44]. Each such wave can be characterized as a fixed point of a "shift and run" map of the type described in [34], but with a continuous shift rather than the discrete one used in [34]. More precisely, we look for lurching waves as fixed points of the map

$$u_{n+1} = P(u_n; \chi, T)$$

where $P(u; \chi, T)$ is defined by taking the function $u(x)$, shifting it in space by an amount χ (to the left if the pattern is moving to the right, recalling that the domain is periodic) and then integrating (3) with this shifted pattern as the initial condition for an amount of time T. A continuous shift is easily implemented in Fourier space. If

$$u(x) = \sum_{n=-M}^{M} a_n e^{inx}$$

then

$$u(x + \chi) = \sum_{n=-M}^{M} \hat{a}_n e^{inx}$$

where $\hat{a}_n = a_n e^{in\chi}$. Note that the stability of a lurching wave can be found from the eigenvalues of the Jacobian of the map P evaluated at the relevant fixed point [34].

It is natural to expect that lurching waves can also be described using a variant of the self-consistency approach. However, so far we have not been able to do this. The main problem is that after time rescaling $v(x,t) = u(x,t/\omega)$ we need to consider Eq. (36) on the functional space

$$\tilde{C}_\chi = \left\{ v \in C([0,2\pi]^2; \mathbb{C}) \; : \; v(x+2\pi, t) = v(x,t), \quad v(x+\chi, t+2\pi) = v(x,t) \right\}$$

and show that for every $F \in \tilde{C}_\chi$ equation (36) has a unique solution $v \in \tilde{C}_\chi$ satisfying $|v| \leq 1$. This turns out to be a nontrivial task due to the nonlocal character of the boundary condition $v(x+\chi, t+2\pi) = v(x,t)$. So we leave it for future investigation.

V. RESULTS

Now we show how the analytical methods developed in Section IV can be used to explain the empirical stability diagrams from Section III. We begin by reviewing the computational efficiency of the two approaches described in Section IV. Then, we show the calculated bifurcation diagrams associated with Figures 2 and 6, which make visible the relationships between various spatiotemporal patterns which are solutions of Eq. (3), sometimes via unstable (and therefore invisible) solutions of this equation.

A. Computational efficiency of the proposed methods

- **Stationary states.** To find stationary states of (3) one could uniformly discretise this in space and solve the corresponding large set of coupled algebraic equations using Newton's method. Or one could solve the system (24). Which method is more efficient depends on the number of spatial points used (call this $\hat{N}$) and M, the number of spatial harmonics used to approximate $F(x)$. If $\hat{N}$ is small and M is large the former method is more efficient, but if $\hat{N}$ is large and M is small the latter method is more efficient. The former method has the advantage that the stability can be readily found from the eigenvalues of the linearisation about the stationary state.

- **Travelling waves.** It was found to be much more efficient to use the approach discussed at the beginning of Sec. IV C, i.e. equation (29), than to solve the system of equations (34). The main reasons for this are (i) the large number of harmonics used to approximate F: we used $M = 50$, giving 101 unknowns, and (ii) the fact that to evaluate the operator $\mathcal{U}$ once we need to numerically integrate (30) four times, as explained in Remark 2. Note that if the kernels W_v and W_s were described exactly by a small number of sinusoidal functions, F could be expressed exactly as a finite Fourier series, with a corresponding small number of unknowns [16, 30].

- **Standing waves.** A standing wave is a periodic solution of (3) and so could be studied using conventional methods after spatial discretisation [42]. This method was found to be much more efficient than the method proposed in Sec. IV D, due to the large number of unknowns required for that method, $(2M+1)(2N+1)$, and the need to integrate (36) four times, as explained above.

B. Bifurcation diagrams for $\kappa_s = 10$

Recall that we found two coexisting stable solutions at $\kappa_v = 1$. We first discuss the standing waves and other related solutions of Eq. (3). The spatially-uniform state is stable for $\kappa_v < 0.96934$ and it undergoes a supercritical Hopf bifurcation with $m = 0$ at this point. The emerging uniformly oscillating state is shown in black in Fig. 8 and is stable upon creation but undergoes a subcritical bifurcation at $\kappa_v = 0.96974$, generating an unstable branch of standing waves, shown in blue in Fig. 8. (This branch of spatially uniform oscillating states is stable only over a very small range of κ_v values and was not observed in Fig. 2.) At $\kappa_v = 0.94185$ a saddle-node bifurcation occurs creating
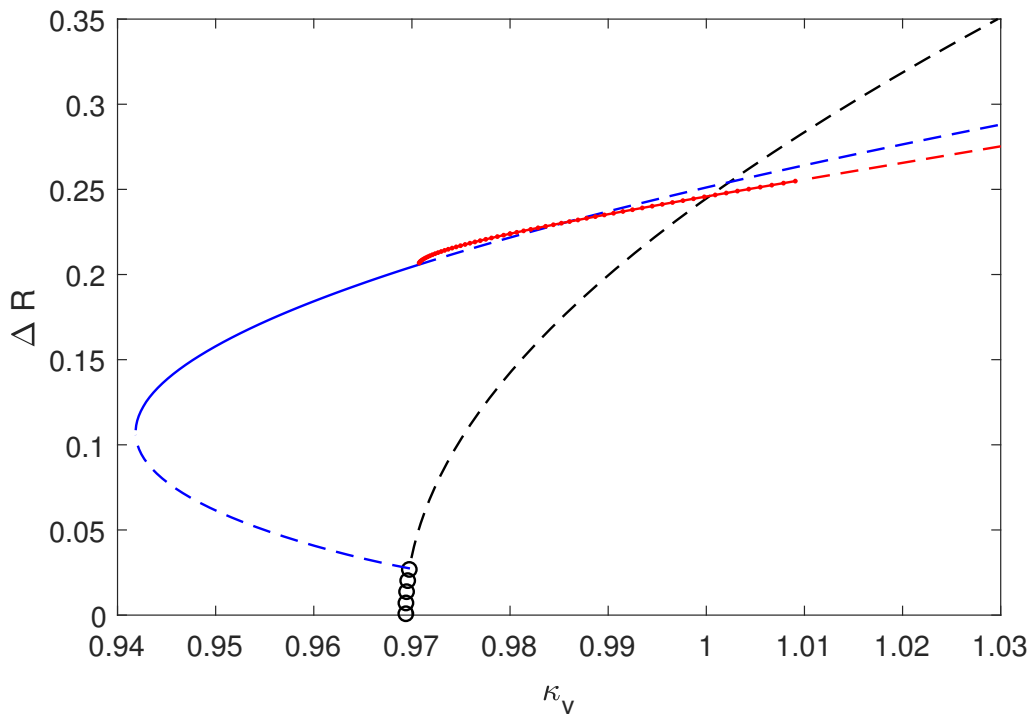
FIG. 8. Bifurcation diagram of standing waves for $\eta_0 = 1$, $\gamma = 0.5$ and $\kappa_s = 10$. Black circles and dashed: spatially-uniform states. Blue solid and dashed: standing waves. Red connected dots and dashed: standing waves with less symmetry. Dashed curves are unstable.

stable and unstable branches of standing waves. At $\kappa_v = 0.97069$ the branch of standing waves undergoes a symmetry breaking bifurcation and a branch of stable standing waves with more complex behavior and less symmetry (shown in red Fig. 8) appears. The latter loses its stability at $\kappa_v = 1.0091$. This analysis provide an explanation for the results shown in the left column of Fig. 2: there is a stable standing wave for smaller values of κ_v and one with less symmetry for larger values.

We now discuss the travelling waves. The travelling wave is stable at $\kappa_v = 0.96$ and either decreasing or increasing κ_v destabilises the wave in a Hopf bifurcation; see Fig. 9. The leftmost bifurcation, at $\kappa_v = 0.95243$, seems subcritical and occurs to the right of the saddle-node bifurcation. Following the branch through the saddle-node bifurcation it terminates in a collision with the spatially unform state at $\kappa_v = 0.9868$. Put another way, the spatially uniform state undergoes a subcritical Hopf bifurcation with $m = 2$ at this parameter value, leading to the creation of an unstable travelling wave — see Fig. 7.

The rightmost Hopf bifurcation of the travelling wave, at $\kappa_v = 0.96398$, is supercritical and results in the creation of a stable lurching solution. We followed this lurching wave and a plot of the spatial shift χ versus κ_v is shown in Fig. 10. The magnitude of χ is small, in keeping with the slow drift mentioned in Sec. III A. These lurching waves remain stable until $\kappa_v = 1.0301$, where they apparently undergo a torus bifurcation, creating a solution which is quasiperiodic in a uniformly travelling coordinate frame. As κ_v grows further, these waves become chaotic. This analysis provide an explanation for the results shown in the right column of Fig. 2: the travelling wave in Fig. 9 has $\Delta R = 0$, the lurching wave is seen at $\kappa_v = 1$, for example, and the quasiperiodic and chaotic behaviour is seen in Fig. 2(d).

C. Bifurcation diagram for $\kappa_s = 20$.

The uniform state undergoes a subcritical Turing bifurcation with $m = 2$ at $\kappa_v = -1.53$ (see Fig. 7). An unstable branch of stationary two-bump solutions emerges at this point, shown dashed in Fig. 11. This solution becomes stable in a saddle-node bifurcation at $\kappa_v = -1.6099$. At $\kappa_v = 0.88565$ a supercritical Hopf bifurcation occurs and a branch of standing waves (or breathing two-bump solutions), shown in blue in Fig. 12 emerges.

These standing waves are stable until a symmetry breaking period-doubling bifurcation at $\kappa_v = 1.0719$. To the right from this point, a branch of standing waves in the form of alternating two-bump patterns is stable, shown in solid red
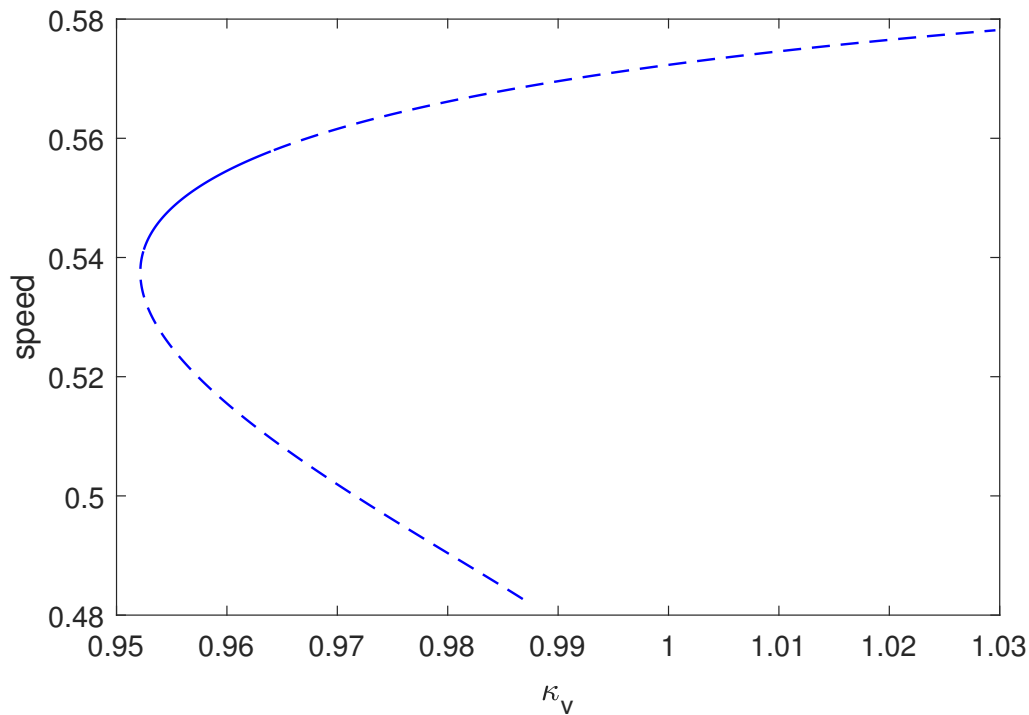
FIG. 9. Bifurcation diagram of travelling waves for $\eta_0 = 1$, $\gamma = 0.5$ and $\kappa_{\rm s} = 10$. Solid: stable; dashed: unstable. The two bifurcations at which the wave loses stability are Hopf bifurcations.

in Fig. 12. At $\kappa_{\rm v} = 1.5563$ this alternating pattern becomes unstable through a supercritical torus bifurcation and a branch of lurching states appears, shown in black in Fig. 12. The lurching state is stable until $\kappa_{\rm v} = 1.6248$. After that it undergoes a sequence of bifurcations leading to a chaotic regime. Note that the branch of periodic solutions shown in blue in Fig. 12 terminates in a collision with an unstable spatially uniform periodic solution (not shown or analysed). This analysis provides an explanation for the results shown in Fig. 6.

VI. DISCUSSION

In this paper, we considered the neural field equation (3), which describes the long-term dynamics of a ring network of QIF neurons with nonlocal synaptic and gap junction coupling, in the limit of a large number of neurons. We showed that apart from spatially uniform states, this model also supports various spatiotemporal patterns, including stationary bump states, standing and travelling waves, and lurching waves. We showed how each of these states can be analyzed semi-analytically using the discretized version of Eq. (3) or using the corresponding self-consistency equation. We believe this to be the first study of spatially extended QIF networks using self-consistency arguments. Finally, we computed detailed bifurcation diagrams for (3), which linked the previous observations together.

The linear stability analysis of constant solutions of Eq. (3) performed in Sec. IV A revealed that there are two qualitatively different bifurcation scenarios for small and large values of synaptic coupling; see Fig. 7. More specifically, for $\kappa_{\rm s} < 13$ the uniform state loses its stability due to the Hopf bifurcation with a spatially uniform eigenfunction, resulting in the creation of a spatially-uniform oscillating state. In contrast, for $\kappa_{\rm s} > 13$ the destabilization of the uniform state occurs due to a Turing bifurcation with a spatially modulated eigenfunction with wave number $m = 2$. This results in the creation of a "two-bump" stationary solution.

Using the algorithms described in Sec. IV, we followed the five types of solutions of Eq. (3) primarily as the parameter $\kappa_{\rm v}$ was varied. This allowed us to better understand the relationship between these solutions and provide an explanation of the numerical results found in Sec. III. More specifically, for $\kappa_{\rm s} = 10$ we found coexisting standing waves and travelling waves, and a type of lurching wave that resulted from a travelling wave undergoing an oscillatory instability. For $\kappa_{\rm s} = 20$ we found the scenario shown in Fig. 12, where more complex solutions are created as $\kappa_{\rm v}$ is increased. Interestingly, the lurching solution found for this value of $\kappa_{\rm s}$ results from a standing wave solution losing stability and starting to travel, hence the increase in χ from zero as $\kappa_{\rm v}$ is increased, shown in Fig. 12(c).

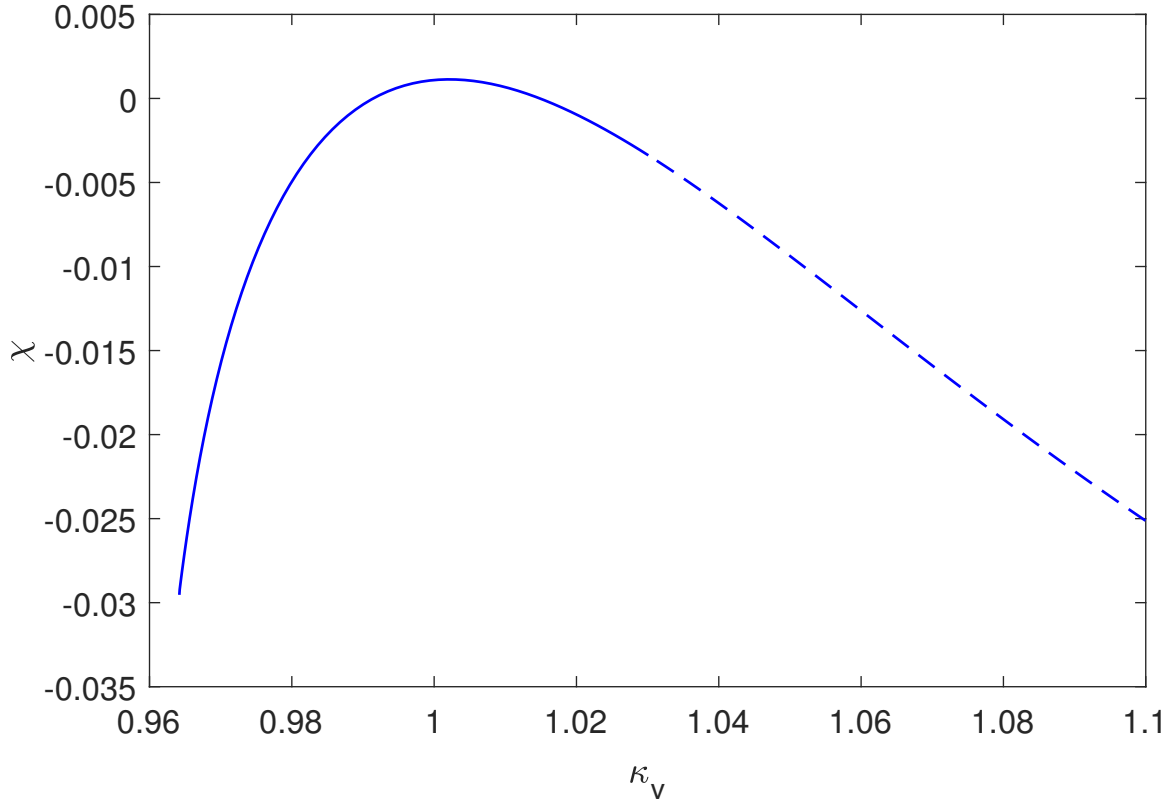The model (3) has many parameters and we have only investigated varying one of them for several values of another.

FIG. 10. Behaviour of lurching waves for $\eta_0 = 1$, $\gamma = 0.5$ and $\kappa_{\mathrm{s}} = 10$. χ is the spatial shift. Solid: stable; dashed: unstable. The left end of the branch of solutions is created in the rightmost bifurcation shown in Fig. 9.

However, our methods could equally-well be used to investigate other variations of parameters. We believe that the numerical and analytical methods of Sec. III and Sec. IV can be extended to other types of networks consisting of QIF neurons, for which stationary, oscillating and moving patterns also define their typical dynamical behaviour. In particular, these methods can be useful for studying two-, three- and higher-dimensional arrays, networks with population structure and networks with propagation delays. Even for the model considered above, it is possible to further investigate which patterns will occur when using other coupling functions $W_{\mathrm{s}}(x)$ and $W_{\mathrm{v}}(x)$, e.g. wrapped Gaussian, exponentially decaying functions, etc. Moreover, it would be interesting to check if these patterns persist in the presence of external noise. In particular, our methods may be able to be generalized to take advantages of the "pseudocumulant" expansions proposed in [45]. We leave these questions for future work.

APPENDIX

Let us consider a complex Riccati equation

$$\frac{dw}{dt} = \gamma + if(t) - g(t)w - iw^2 \tag{45}$$

with a parameter $\gamma \in \mathbb{R}$ and real-valued functions $f(t)$ and $g(t)$. In this section, we show that for $\gamma > 0$ all solutions of Eq. (45) have special invariance properties with respect to the complex half-plane

$$\mathbb{P} = \{w \in \mathbb{C} \ : \ \mathrm{Re}\ w > 0\}.$$

In order to proceed, we recall that the complex plane transformation

$$z = \frac{1-w}{1+w} \tag{46}$$

maps the half-plane $\mathbb{P}$ onto the unit disc

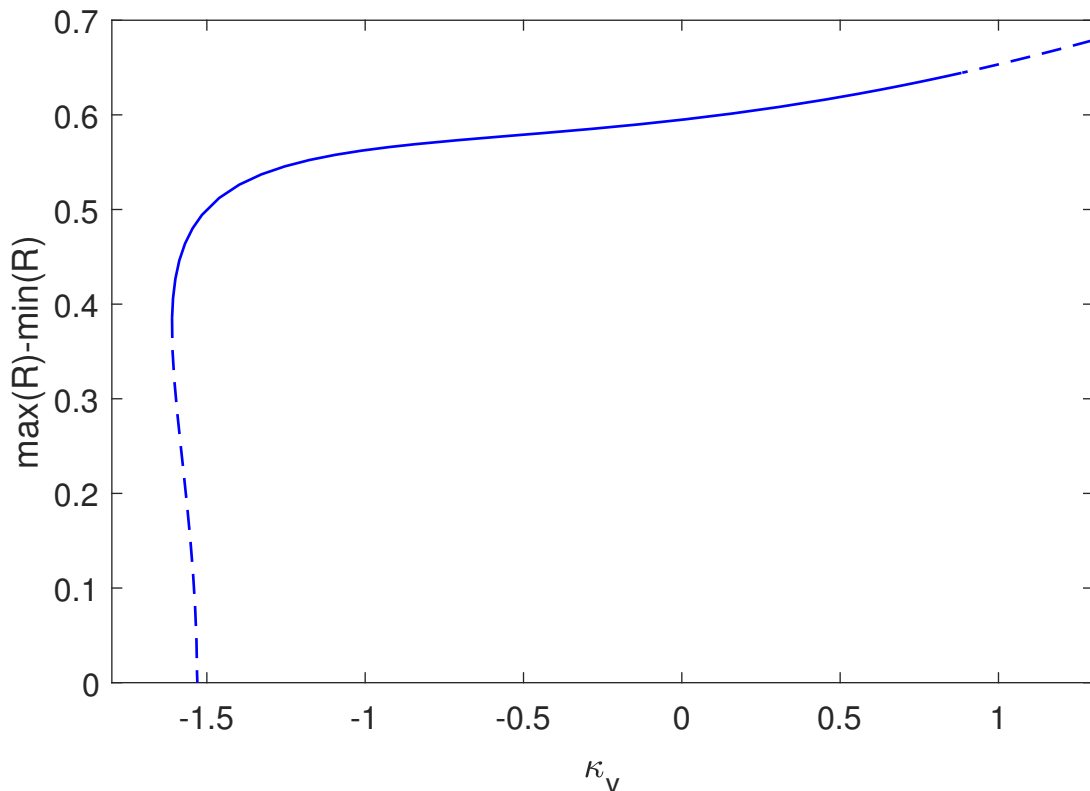$$\mathbb{D} = \{z \in \mathbb{C} \ : \ |z| < 1\}.$$

FIG. 11. Stationary two-bump solution $\eta_0 = 1$, $\gamma = 0.5$ and $\kappa_s = 20$. Solid: stable; dashed: unstable. The vertical axis shows $\max_x R(x) - \min_x R(x)$. The solution is stable between the saddle-node bifurcation and a supercritical Hopf bifurcation at $\kappa_v = 0.88565$. (Note that negative values of κ_v are unphysical, but we plot them to show the full branch of solutions.)

Moreover, using formula (46) as a change of variable, we can rewrite Eq. (45) in an equivalent form

$$\frac{dz}{dt} = -\frac{\gamma + if(t)}{2}(1+z)^2 + \frac{g(t)}{2}(1-z^2) + \frac{i}{2}(1-z)^2. \tag{47}$$

Then, it is easy to see that Eq. (47) is a complex Riccati equation

$$\frac{dz}{dt} = c_0(t) + c_1(t)z + c_2(t)z^2$$

with

$$c_0(t) = \frac{-\gamma - if(t) + g(t) + i}{2}, \quad c_1(t) = -\gamma - if(t) - i, \quad c_2(t) = \frac{-\gamma - if(t) - g(t) + i}{2}.$$

Therefore, Proposition 2 from [16] implies that for every $\gamma > 0$ and for all real 2π-periodic continuous functions $f(t)$ and $g(t)$, Eq. (47) has exactly one stable 2π-periodic solution and this solution satisfies $|z(t)| < 1$ for all $0 \le t \le 2\pi$. Moreover, using the main argument of the proof of Proposition 2 in [16], we can show that every solution of Eq. (47) with an initial condition in $\mathbb{D}$ remains in this unit disc for any finite time interval.

Due to the equivalence between the solutions of Eq. (45) and the solutions of Eq. (47), we can reformulate the above results as follows.

Proposition 2 *Suppose that $\gamma > 0$ and $f(t)$, $g(t)$ are real 2π-periodic continuous functions.*

(i) Then for every $w_0 \in \mathbb{P}$ the complex Riccati equation (45) with initial condition $w(0) = w_0$ has a solution $w(t)$, which is bounded on the interval $[0, 2\pi]$ and satisfies $\operatorname{Re} w(t) > 0$.

(ii) Moreover, Eq. (45) has exactly one stable 2π-periodic solution and this solution satisfies $\operatorname{Re} w(t) > 0$ for all $0 \le t \le 2\pi$.

Since Eq. (45) belongs to the class of complex Riccati equations its Poincaré map coincides with a Möbius transformation, see [46, 47]. This fact can be used to speed up the computation of periodic solutions of Eq. (45).
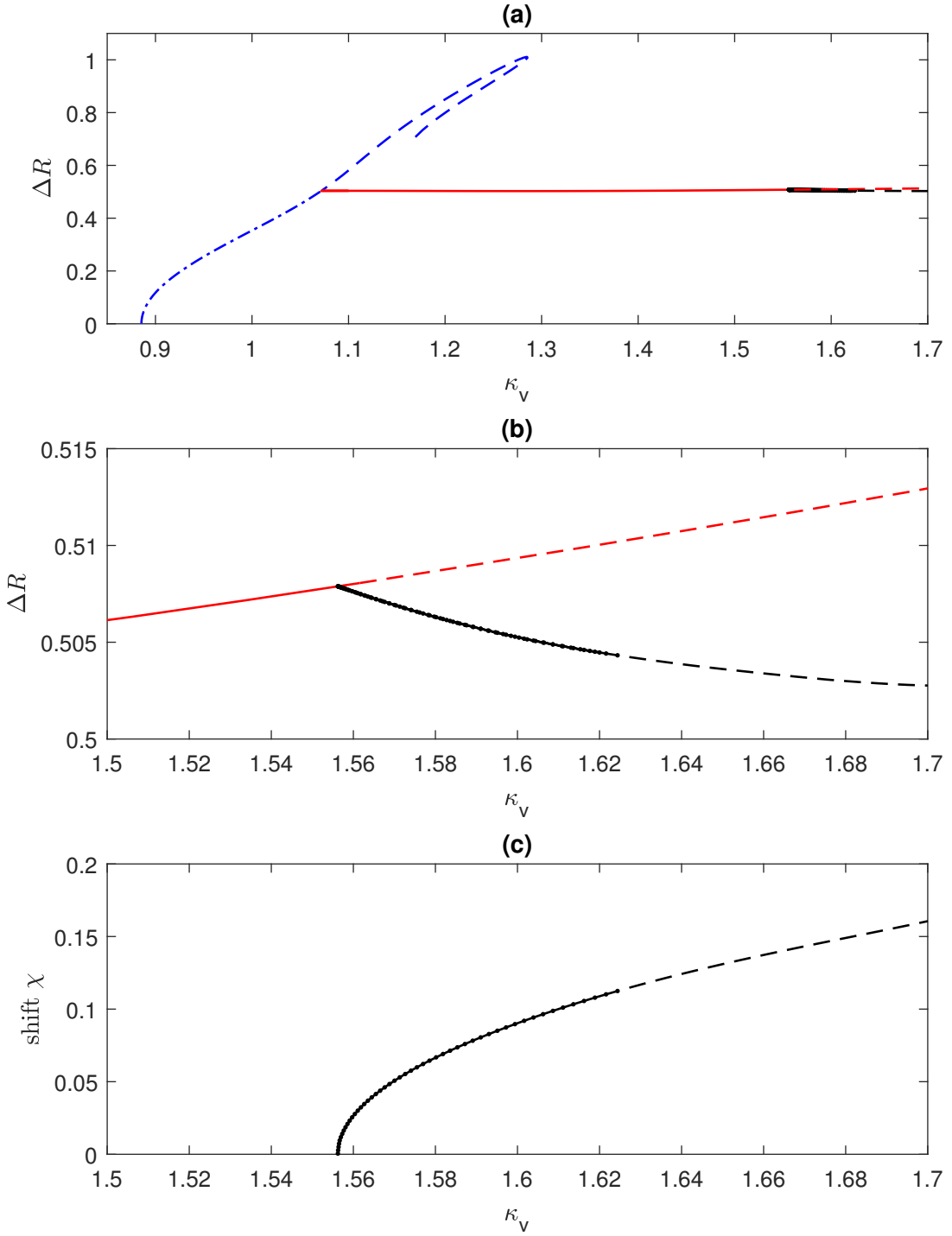
FIG. 12. Bifurcation diagrams for $\kappa_{\mathrm{s}} = 20$. Blue dash-dotted and dashed: periodic solution. Red solid and dashed: period-doubled solution. Black connected dots and dashed: lurching solution. Dashed curves are unstable. Panel (b) is an enlargment of panel (a). Panel (c) shows the shift, χ, of the lurching solution.

Remark 2 *If the conditions of Proposition 2 are fulfilled, then the stable solution of Eq. (45) can be computed in the following way.*

(i) One solves Eq. (45) on the interval $t \in (0, 2\pi]$ with three different initial conditions $w(0) = w_k \in \mathbb{P}$, $k = 1, 2, 3$, and obtains three solutions $W_k(t)$. Since each w_k lies in the half-plane $\mathbb{P}$ this automatically implies that $W_k(t)$ is bounded on the interval $t \in [0, 2\pi]$. Note that this fact is not obvious a priori, since some of the solutions of Eq. (45)

blow up in finite time.

(ii) One denotes $\zeta_k = W_k(2\pi)$. Then, due to the properties of Poincaré map one has $\zeta_k = \mathcal{M}(w_k)$, $k = 1, 2, 3$, where $\mathcal{M}(w)$ is a Möbius transformation representing this map. The above three relations can be used to reconstruct the map $\mathcal{M}(w)$, namely

$$\mathcal{M}(w) = \frac{aw + b}{cw + d}$$

where

$$a = \det \begin{pmatrix} w_1\zeta_1 & \zeta_1 & 1 \\ w_2\zeta_2 & \zeta_2 & 1 \\ w_3\zeta_3 & \zeta_3 & 1 \end{pmatrix}, \quad b = \det \begin{pmatrix} w_1\zeta_1 & w_1 & \zeta_1 \\ w_2\zeta_2 & w_2 & \zeta_2 \\ w_3\zeta_3 & w_3 & \zeta_3 \end{pmatrix},$$

$$c = \det \begin{pmatrix} w_1 & \zeta_1 & 1 \\ w_2 & \zeta_2 & 1 \\ w_3 & \zeta_3 & 1 \end{pmatrix}, \quad d = \det \begin{pmatrix} w_1\zeta_1 & w_1 & 1 \\ w_2\zeta_2 & w_2 & 1 \\ w_3\zeta_3 & w_3 & 1 \end{pmatrix}.$$

(iii) Once the map $\mathcal{M}(w)$ is known, one can find its fixed points by solving the quadratic equation

$$cw^2 + dw - aw - b = 0.$$

This yields two roots

$$w_\pm = \frac{a - d \pm \sqrt{(a - d)^2 + 4bc}}{2c}.$$

(iv) Choosing from the roots w_+ and w_- the one that lies in the half-plane $\mathbb{P}$, one obtains the initial condition that determines the periodic solution of interest. The latter can be computed by solving Eq. (45) with this initial condition.

(v) Sometime it may happen that the Poincaré map $\mathcal{M}(w)$ is strongly contracting so that

$$|\zeta_1 - \zeta_2| + |\zeta_3 - \zeta_2| < 10^{-8},$$

where the value 10^{-8} is chosen through experience. In this case, the calculations in steps (ii) and (iii) become inaccurate. Then the initial condition of the periodic solution of interest is approximately given by the average $(\zeta_1 + \zeta_2 + \zeta_3)/3$.

The above steps (i)–(v) can be understood as a constructive definition of the solution operator of Eq. (45), which for every $\gamma > 0$ and all real 2π-periodic coefficients $f(t)$ and $g(t)$ yields the corresponding stable 2π-periodic solution of Eq. (45).

Proposition 3 *For constant coefficients f and g, Eq. (45) has a single fixed point satisfying $\mathrm{Re}\,(w) \geq 0$. This fixed point is determined by the formula*

$$w = \mathcal{S}(f, g, \gamma) := \frac{1}{2}\sqrt{\frac{\sqrt{(g^2 - 4f)^2 + 16\gamma^2} - g^2 + 4f}{2}} + \frac{i}{2}\left(g - \sqrt{\frac{\sqrt{(g^2 - 4f)^2 + 16\gamma^2} + g^2 - 4f}{2}}\right). \tag{48}$$

Proof: Any fixed point of Eq. (45) satisfies

$$\gamma + if - gw - iw^2 = 0.$$

This quadratic equation has two solutions

$$w = -\frac{1}{2i}\left(g \pm \sqrt{g^2 + 4i(\gamma + if)}\right) = \frac{i}{2}\left(g \pm \sqrt{g^2 - 4f + 4i\gamma}\right). \tag{49}$$

Since $\gamma > 0$, de Moivre's formula yields

$$g^2 - 4f + 4i\gamma = \sqrt{(g^2 - 4f)^2 + 16\gamma^2}\left(\cos\left(\text{arccot}\frac{g^2 - 4f}{4\gamma}\right) + i\sin\left(\text{arccot}\frac{g^2 - 4f}{4\gamma}\right)\right).$$

Hence

$$\sqrt{g^2 - 4f + 4i\gamma} = \sqrt[4]{(g^2 - 4f)^2 + 16\gamma^2}\left(\cos\left(\frac{1}{2}\text{arccot}\frac{g^2 - 4f}{4\gamma}\right) + i\sin\left(\frac{1}{2}\text{arccot}\frac{g^2 - 4f}{4\gamma}\right)\right).$$

Using the half-angle formulas and the identity

$$\cos\left(\text{arccot}\frac{g^2 - 4f}{4\gamma}\right) = \frac{g^2 - 4f}{\sqrt{(g^2 - 4f)^2 + 16\gamma^2}},$$

we rewrite this as follows

$$\sqrt{g^2 - 4f + 4i\gamma} = \sqrt{\frac{\sqrt{(g^2 - 4f)^2 + 16\gamma^2} + g^2 - 4f}{2}} + i\sqrt{\frac{\sqrt{(g^2 - 4f)^2 + 16\gamma^2} - g^2 + 4f}{2}}.$$

Inserting this expression into (49) and choosing the sign of the square root that ensures the inequality $\text{Re}(w) \geq 0$, we obtain formula (48). ∎

ACKNOWLEDGEMENTS

---

[1] G.B. Ermentrout and D. Terman. *Mathematical Foundations of Neuroscience*, volume 35. Springer Verlag, 2010.
[2] Stephen Coombes and Kyle CA Wedgwood. *Neurodynamics: An Applied Mathematics Perspective*, volume 75. Springer Nature, 2023.
[3] Stephen Coombes, Peter beim Graben, Roland Potthast, and James Wright, editors. *Neural Fields: Theory and Applications*. Springer, 2014.
[4] Paul C Bressloff. Spatiotemporal dynamics of continuum neural fields. *Journal of Physics A: Mathematical and Theoretical*, 45(3):033001, 2012.
[5] Áine Byrne, James Ross, Rachel Nicks, and Stephen Coombes. Mean-field models for EEG/MEG: from oscillations to waves. *Brain topography*, 35(1):36–53, 2022.
[6] B. Ermentrout. Neural networks as spatio-temporal pattern-forming systems. *Rep. Prog. Phys.*, 61:353–430, 1998.
[7] Klaus Wimmer, Duane Q Nykamp, Christos Constantinidis, and Albert Compte. Bump attractor dynamics in prefrontal cortex explains behavioral precision in spatial working memory. *Nature neuroscience*, 17(3):431–439, 2014.
[8] David Horn and Irit Opher. Solitary waves of integrate-and-fire neural fields. *Neural Comput.*, 9(8):1677–1690, 1997.
[9] Shun-ichi Amari. Dynamics of pattern formation in lateral-inhibition type neural fields. *Biological cybernetics*, 27(2):77–87, 1977.
[10] Carlo R Laing and William C Troy. Two-bump solutions of amari-type models of neuronal pattern formation. *Physica D: Nonlinear Phenomena*, 178(3-4):190–218, 2003.
[11] Hugh R Wilson and Jack D Cowan. A mathematical theory of the functional dynamics of cortical and thalamic nervous tissue. *Kybernetik*, 13(2):55–80, 1973.
[12] S. Coombes. Waves, bumps, and patterns in neural field theories. *Biol. Cybern.*, 93(2):91–108, 2005.
[13] Carlo R Laing. Exact neural fields incorporating gap junctions. *SIAM Journal on Applied Dynamical Systems*, 14(4):1899–1929, 2015.
[14] Oleh Omel'chenko and Carlo R Laing. Collective states in a ring network of theta neurons. *Proceedings of the Royal Society A*, 478(2259):20210817, 2022.
[15] Carlo R Laing. Derivation of a neural field model from a network of theta neurons. *Physical Review E*, 90(1):010901, 2014.
[16] Carlo R Laing and Oleh E Omel'chenko. Periodic solutions in next generation neural field models. *Biological Cybernetics*, 117(4):259–274, 2023.
[17] Jose M. Esnaola-Acebes, Alex Roxin, Daniele Avitabile, and Ernest Montbrió. Synchrony-induced modes of oscillation of a neural field model. *Phys. Rev. E*, 96:052407, Nov 2017.
[18] Helmut Schmidt and Daniele Avitabile. Bumps and oscillons in networks of spiking neurons. *Chaos*, 30:033133, 2020.

[19] Áine Byrne, Daniele Avitabile, and Stephen Coombes. Next-generation neural field model: The evolution of synchrony within patterns and waves. *Phys. Rev. E*, 99:012313, Jan 2019.

[20] Albert Compte, Nicolas Brunel, Patricia S. Goldman-Rakic, and Xiao-Jing Wang. Synaptic mechanisms and network dynamics underlying spatial working memory in a cortical network model. *Cerebral Cortex*, 10(9):910–923, 2000.

[21] Xiaohui Xie, Richard HR Hahnloser, and H Sebastian Seung. Double-ring network model of the head-direction system. *Physical Review E*, 66(4):041902, 2002.

[22] Mikail Khona and Ila R Fiete. Attractor and integrator networks in the brain. *Nature Reviews Neuroscience*, 23(12):744–766, 2022.

[23] David J Pinto and G Bard Ermentrout. Spatially structured activity in synaptically coupled neuronal networks: I. Traveling fronts and pulses. *SIAM journal on Applied Mathematics*, 62(1):206–225, 2001.

[24] Paul C Bressloff and Matthew A Webber. Neural field model of binocular rivalry waves. *Journal of computational neuroscience*, 32(2):233–252, 2012.

[25] Xiaoying Huang, William C Troy, Qian Yang, Hongtao Ma, Carlo R Laing, Steven J Schiff, and Jian-Young Wu. Spiral waves in disinhibited mammalian neocortex. *Journal of Neuroscience*, 24(44):9897–9902, 2004.

[26] Bard Ermentrout, Jonathan Rubin, and Remus Osan. Regular traveling waves in a one-dimensional network of theta neurons. *SIAM Journal on Applied Mathematics*, 62(4):1197–1221, 2002.

[27] Paul C Bressloff and Samuel R Carroll. Laminar neural field model of laterally propagating waves of orientation selectivity. *PLoS computational biology*, 11(10):e1004545, 2015.

[28] Stefanos E Folias and Paul C Bressloff. Breathing pulses in an excitatory neural network. *SIAM Journal on Applied Dynamical Systems*, 3(3):378–407, 2004.

[29] Ernest Montbrió, Diego Pazó, and Alex Roxin. Macroscopic description for networks of spiking neurons. *Phys. Rev. X*, 5:021028, Jun 2015.

[30] O. E. Omel'chenko. Periodic orbits in the ott-antonsen manifold. *Nonlinearity*, 36:845–861, 2023.

[31] M. Bataille-Gonzalez, M. G. Clerc, E. Knobloch, and O. E. Omel'chenko. Traveling spiral wave chimeras in coupled oscillator systems: emergence, dynamics, and transitions. *New Journal of Physics*, 25(10):103023, 2023.

[32] Bastian Pietras, Federico Devalle, Alex Roxin, Andreas Daffertshofer, and Ernest Montbrió. Exact firing rate model reveals the differential effects of chemical versus electrical synapses in spiking networks. *Physical Review E*, 100(4):042412, 2019.

[33] Ernest Montbrió and Diego Pazó. Exact mean-field theory explains the dual role of electrical synapses in collective synchronization. *Physical review letters*, 125(24):248101, 2020.

[34] Thomas M Wasylenko, Jaime E Cisternas, Carlo R Laing, and Ioannis G Kevrekidis. Bifurcations of lurching waves in a thalamic neuronal network. *Biological cybernetics*, 103(6):447–462, 2010.

[35] S Coombes. Dynamics of synaptically coupled integrate-and-fire-or-burst neurons. *Physical Review E*, 67(4):041910, 2003.

[36] David Golomb and G Bard Ermentrout. Continuous and lurching traveling pulses in neuronal networks with delay and spatially decaying connectivity. *Proceedings of the National Academy of Sciences*, 96(23):13480–13485, 1999.

[37] David Golomb and G Bard Ermentrout. Effects of delay on the type and velocity of travelling pulses in neuronal networks with spatially decaying connectivity. *Network: Computation in Neural Systems*, 11(3):221, 2000.

[38] David Golomb and G Bard Ermentrout. Bistability in pulse propagation in networks of excitatory and inhibitory populations. *Physical Review Letters*, 86(18):4179, 2001.

[39] Alice C Yew, DH Terman, and G Bard Ermentrout. Propagating activity patterns in thalamic neuronal networks. *SIAM Journal on Applied Mathematics*, 61(5):1578–1604, 2001.

[40] O. E. Omel'chenko. Mathematical framework for breathing chimera states. *Journal of Nonlinear Science*, 32(2):1–34, 2022.

[41] Carlo R Laing, William C Troy, Boris Gutkin, and G Bard Ermentrout. Multiple bumps in a neuronal model of working memory. *SIAM Journal on Applied Mathematics*, 63(1):62–97, 2002.

[42] Carlo R Laing. Numerical bifurcation theory for high-dimensional neural models. *The Journal of Mathematical Neuroscience*, 4(1):13, 2014.

[43] Carlo R Laing and Oleh Omel'chenko. Moving bumps in theta neuron networks. *Chaos: An Interdisciplinary Journal of Nonlinear Science*, 30(4):043117, 2020.

[44] Björn Sandstede and Arnd Scheel. On the structure of spectra of modulated travelling waves. *Mathematische Nachrichten*, 232(1):39–93, 2001.

[45] Denis S Goldobin, Matteo Di Volo, and Alessandro Torcini. Reduction methodology for fluctuation driven population dynamics. *Physical Review Letters*, 127(3):038301, 2021.

[46] J. Campos. Möbius transformations and periodic solutions of complex Riccati equations. *Bull. London Math. Soc.*, 29:205–215, 1997.

[47] P. Wilczyński. Planar nonautonomous polynomial equations: the Riccati equation. *J. Differ. Equ.*, 244:1304–1328, 2008.